Hemispheric Dichotomy in Lithosphere Thickness on Mars Caused by Differences in Crustal Structure and Composition

Melanie Thiriet, Chloé Michaut, Doris Breuer, Ana-Catalina Plesa

AGU100 ADVANCING EARTH AND SPACE SCIENCE

JGR

Journal of Geophysical Research: Planets

RESEARCH ARTICLE
10.1002/2017JE005431

Key Points:
- With 1-D thermal evolution models in Monte Carlo simulations we find north/south crustal properties that fit Mars's elastic thickness estimates
- Our results suggest that 55–65% of the bulk radioelement content are in the crust, mostly in the southern one (43–51%)
- We retrieve a north/south surface heat flux of 17.1–19.5 mW/m^2 and 24.8–26.5 mW/m^2, respectively, that could influence InSight measurements

Correspondence to:
M. Thiriet,
thiriet@ipgp.fr

Citation:
Thiriet, M., Michaut, C., Breuer, D., & Plesa, A.-C. (2018). Hemispheric dichotomy in lithosphere thickness on Mars caused by differences in crustal structure and composition. *Journal of Geophysical Research: Planets*, *123*, 823–848. https://doi.org/10.1002/2017JE005431

Received 28 AUG 2017
Accepted 22 FEB 2018
Accepted article online 1 MAR 2018
Published online 6 APR 2018

Hemispheric Dichotomy in Lithosphere Thickness on Mars Caused by Differences in Crustal Structure and Composition

Mélanie Thiriet[1], **Chloé Michaut**[1,2], **Doris Breuer**[3], **and Ana-Catalina Plesa**[3]

[1]Université Paris Diderot, Institut de Physique du Globe de Paris, Sorbonne Paris Cité, Paris, France, [2]Université de Lyon, Laboratoire de Géologie, Terre, Planète, Environnement, École Normale Supérieure de Lyon, Lyon, France, [3]Institute of Planetary Research, German Aerospace Center (DLR), Berlin, Germany

Abstract Estimates of the Martian elastic lithosphere thickness suggest small values of ~25 km during the Noachian for the southern hemisphere and a large present-day difference below the two polar caps (≥300 km in the north and > 110 km in the south). In addition, young lava flows suggest that Mars has been volcanically active up to the recent past. We run Monte Carlo simulations using a 1-D parameterized thermal evolution model to investigate whether a north/south hemispheric dichotomy in crustal properties and composition can explain these constraints. Our results suggest that 55–65% of the bulk radioelement content are in the crust, and most of it (43–51%) in the southern one. The southern crust can be up to 480 kg/m^3 less dense than the northern one and might contain a nonnegligible proportion of felsic rocks. Our models predict a dry mantle and a wet or dry crustal rheology today. This is consistent with a mantle depleted in radioelements and volatiles. We retrieve north/south surface heat flux of 17.1–19.5 mW/m^2 and 24.8–26.5 mW/m^2, respectively, and a large difference in lithospheric temperatures between the two hemispheres (170–304 K in the shallow mantle). This difference could leave a signature in the seismic signals measured by the future InSight mission.

1. Introduction

In the absence of direct heat flux measurements, the thermal and geodynamic history of Mars still remains enigmatic. Indirect evidence for the evolution of the Martian heat flux with time is offered by elastic lithosphere thickness estimates. They represent a measure of the amount of stress the lithosphere can sustain before yielding, either by brittle deformation in the upper cold part of the lithosphere or by ductile deformation in the hotter lower one. Elastic lithosphere thicknesses are sensitive to the lithosphere thermal structure providing heat flow estimates. They have been mainly derived by local analysis of topography and gravity data, in particular, below large volcanic loads (Belleguic et al., 2005; Grott et al., 2011; Hoogenboom & Smrekar, 2006; Kiefer, 2004; McGovern et al., 2004; Ritzer & Hauck, 2009; Wieczorek, 2008). Other methods have also been used. In particular, elastic lithosphere thicknesses have been estimated for the polar regions by modeling the deflection under the cap load and comparing it with the deflection measured by the Shallow Radar on board the Mars Reconnaissance orbiter (Phillips et al., 2008). Finally, indications on local elastic lithosphere thicknesses have been derived from local geomorphological features such as rift uplift (Barnett & Nimmo, 2002; Grott et al., 2005; Kronberg et al., 2007) or from estimates of the seismogenic layer thickness on thrust faults (Grott et al., 2007; Ruiz et al., 2008; Schultz & Watters, 2001). As elastic thicknesses have been estimated for different ages—the age of the deformed surface or load—they provide an overview of Mars thermal evolution.

Elastic lithosphere thicknesses on Mars were very low (~20 km) during the Noachian, and increased above 50 km during the Hesperian to finally reach values between 40 and 150 km in the Amazonian, reflecting a progressive cooling of the planet (Grott & Breuer, 2008; Grott et al., 2013). However, the very large present-day thickness of ≥300 km estimated below the north polar cap (Phillips et al., 2008) seems hard to reconcile with these other values. Using a 1-D parameterized thermal model, Grott and Breuer (2009) showed that present-day values ≥300 km can only be explained if Mars has a subchondritic bulk composition for a moderate crustal enrichment in heat sources. Moreover, they found that present-day melt formation below large volcanoes (Hartmann & Malin, 2000; Hartmann et al., 1999; Neukum et al., 2004; Werner, 2009) requires either

a strongly pressure dependent mantle viscosity or endothermic phase transitions in the case of a dry mantle rheology, or large mantle water contents of the order of 1,000 ppm if a wet mantle rheology is considered. In the framework of a 1-D model, such a large present-day elastic thickness is incompatible with the very small Noachian values (Grott & Breuer, 2009). Moreover the north pole value is significantly larger than the present-day elastic lithosphere thickness suggested below the southern polar cap (only 161 km, though any value higher than 110 km could fit the observations, Wieczorek, 2008).

This discrepancy between different estimates of elastic lithosphere thickness was attributed to spatial variability that cannot be resolved with classical 1-D thermal models (Grott & Breuer, 2009). Grott and Breuer (2010) provided an explanation for the large present-day elastic thickness by including the effects of thermal anomalies in a 1-D parameterized model. However, their model relies on a number of assumptions related to mantle thermal anomalies. The 2-D and 3-D thermal models by Kiefer and Li (2009) and Plesa et al. (2016) allow to investigate these spatial variations self-consistently, but are extremely time consuming and therefore inappropriate to explore a large range of parameters. In addition, the elastic thickness is very sensitive to lithosphere thermal structure and thus to crustal thermal properties (enrichment in radioelements, thermal conductivity), which can show spatial variations. Furthermore, Mars bulk content in radioelements and their distribution between the mantle and crust remain poorly constrained but play a major role in the planet thermal evolution (Grott & Breuer, 2009; Sekhar & King, 2014). It seems therefore essential to investigate the potential effect of spatial differences in crustal enrichment and properties on elastic lithosphere thickness evolution.

As a potential source of spatial crustal differences, the hemispheric dichotomy of Mars is a major candidate. The southern highlands are characterized by sharp reliefs more craterized and superficially older than the northern lowlands covered by extensive lava plains. These latter are very flat and lower in altitude by ~6 km compared to the southern hemisphere. At the dichotomy boundary, the large volcano complexes of Tharsis and Elysium rise are present. As the dichotomy predates the formation of the volcanic regions, their belonging to one of the two hemispheres remains uncertain. Andrews-Hanna et al. (2008) argue for a location in the northern hemisphere and a lowland surface fraction of 42%.

The origin of this surface dichotomy remains debated and various formation mechanisms have been proposed such as a heterogeneous fractionation of an early magma ocean (Solomon et al., 2005), a mantle overturn (Elkins-Tanton et al., 2005), a degree 1 mantle convection pattern (Roberts & Zhong, 2006; Yoshida & Kageyama, 2006), or an impact origin either in the north (Andrews-Hanna et al., 2008; Marinova et al., 2008) or in the south (Golabek et al., 2011; Leone et al., 2014; Reese et al., 2010). In any case, the dichotomy formation would probably date back to the early stages of Mars evolution, between 4.5 and 4 Gyr (Bottke & Andrews-Hanna, 2017; Brasser & Mojzsis, 2017; Frey, 2008; Nimmo & Tanaka, 2005; Nyquist et al., 2001). The dichotomy in topography is likely compensated by a difference in crustal thickness and/or density.

Despite the large north/south dichotomy, the surface of Mars seems nearly homogeneous in composition. The analysis of SNC (Shergottites, Nakhlites, Chassignites) meteorites (Agee et al., 2013; Aoudjehane et al., 2012; Humayun et al., 2013; McSween et al., 2006) and spectroscopic investigations of the surface (Baratoux et al., 2011; Christensen et al., 2005; Mustard et al., 2005) point to a basaltic composition. The surface distribution in radioelements seems roughly uniform (Taylor et al., 2006), with no clear north/south difference. These observations lead to the traditional Mars crustal model where the crust has uniform properties except that the southern one is thicker to compensate for its higher altitude, implying a higher bulk radioelement content and thus a hotter lithosphere in the south.

However, recent studies have shown that the southern and northern crusts could potentially have different properties. In particular, evidence of felsic rocks, such as anorthosites and granodiorites, has been found by remote-sensing techniques (Carter & Poulet, 2013; Wray et al., 2013) or in situ analysis in the Gale crater (Sautter et al., 2015). This felsic material is located in the southern hemisphere (see Figure 1), and has been identified in rocks excavated from depth in crater rims and crater floors, suggesting the potential presence of a reservoir enriched in silica and buried within the southern crust (Baratoux et al., 2014; Carter & Poulet, 2013; Pauer & Breuer, 2008; Sautter et al., 2015; Wray et al., 2013). Furthermore, the bulk crustal density is largely debated. While Goossens et al. (2017) has estimated a very low average density of $2,582 \pm 209$ kg/m^3, Baratoux et al. (2014), on the contrary, proposed a value larger than 3,100 kg/m^3. Such a large value would imply a very thick southern crust, hardly reconciliable with geoid-to-topography ratios without the existence of a less dense component in the south (Baratoux et al., 2014). A difference in composition between the northern

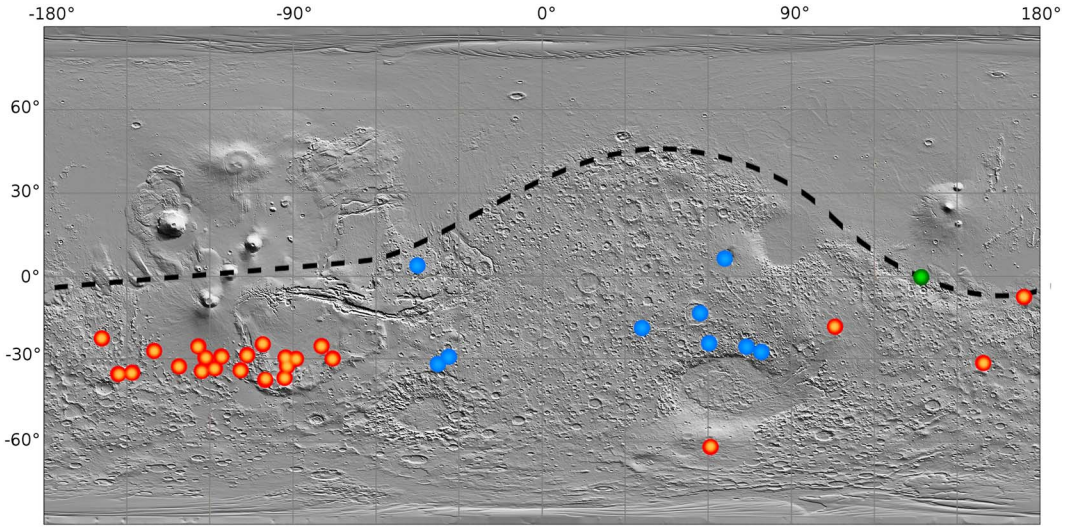

Figure 1. Indications of potential north/south differences in crustal properties over a Mars Orbiter Laser Altimeter-shaded relief topographic map. The boundary of the north/south dichotomy proposed by Andrews-Hanna et al. (2008) is represented by the dashed line. Red points indicate ancient volcanoes detected by Xiao et al. (2012) and Huang and Xiao (2014). Blue points show the localization of felsic rocks detected by Carter and Poulet (2013) and Wray et al. (2013). Felsic rocks very similar to that characterizing the early terrestrial continental crust have been detected with the Curiosity rover in the Gale crater (green point) (Sautter et al., 2015). All these detections are located in the southern highlands.

and southern crusts would also suggest a difference in radioactive element content. In particular, Mars's anorthosites could result from magmatic processes that produce highly evolved melts, implying a larger radioelement enrichment in the southern buried felsic component. Moreover, a recent study suggested that the thermal properties of surface rocks vary with their age (Bandfield et al., 2013). The north is covered by compact lava flows (Bandfield et al., 2013; Huang & Xiao, 2014; Xiao et al., 2012), while the old surface of the southern hemisphere is made of fine particulate and poorly consolidated materials from ancient explosive volcanism or widespread ejecta deposition following a large impact (Figure 1). Due to the presence of these porous materials, thermal conductivity in the southern hemisphere could be lower (Piqueux & Christensen, 2009a, 2009b) than that in the north over several kilometers. This difference in thermal conductivity might disappear at depth by compaction.

Here we test two plausible crustal models: one with a southern crust potentially less conductive for its upper part, enriched in radioelements and silica compared to that of the northern hemisphere, and a more traditional one where the north and south have the same crustal properties except that the southern crust is thicker. Using 1-D parameterized thermal evolution models of Mars accounting for two hemispheres with different crustal models in Monte Carlo simulations, we constrain the thermal parameters of the northern and southern crusts (thickness, radioelement enrichment, and density) that allow to fit elastic lithosphere thickness estimates at different ages.

2. Constraints on the Thickness of the Elastic Lithosphere

In this study, we use elastic lithosphere thickness (T_e) estimates, previously compiled by Grott and Breuer (2008) and Grott et al. (2013), as the main constraints for the parameters of our models (Figure 2b). First, we distinguish between estimates in the northern or southern hemispheres. We notice that the low values in the Noachian reported by Grott and Breuer (2008) are mostly located in the southern hemisphere. These estimates are all in the range 10 to 37 km, although values in the range 0 and 50 km between 4.2 and 3.5 Gyr can fit given error bars and age scattering (Grott et al., 2013; McGovern et al., 2004). Elastic thickness estimates in the Noachian are not well constrained in the northern hemisphere. On the one hand, Hoogenboom and Smrekar (2006) provide very low estimates, comparable to those in the south, that are likely associated to large uncertainties as they are based on topography and gravity data analyses in a region where evidence of past topography has mostly been erased. On the other hand, Ritzer and Hauck (2009) retrieve a range estimate of 100–180 km at Isidis Planitia, at the edge of the highlands/lowlands boundary. Elastic thicknesses

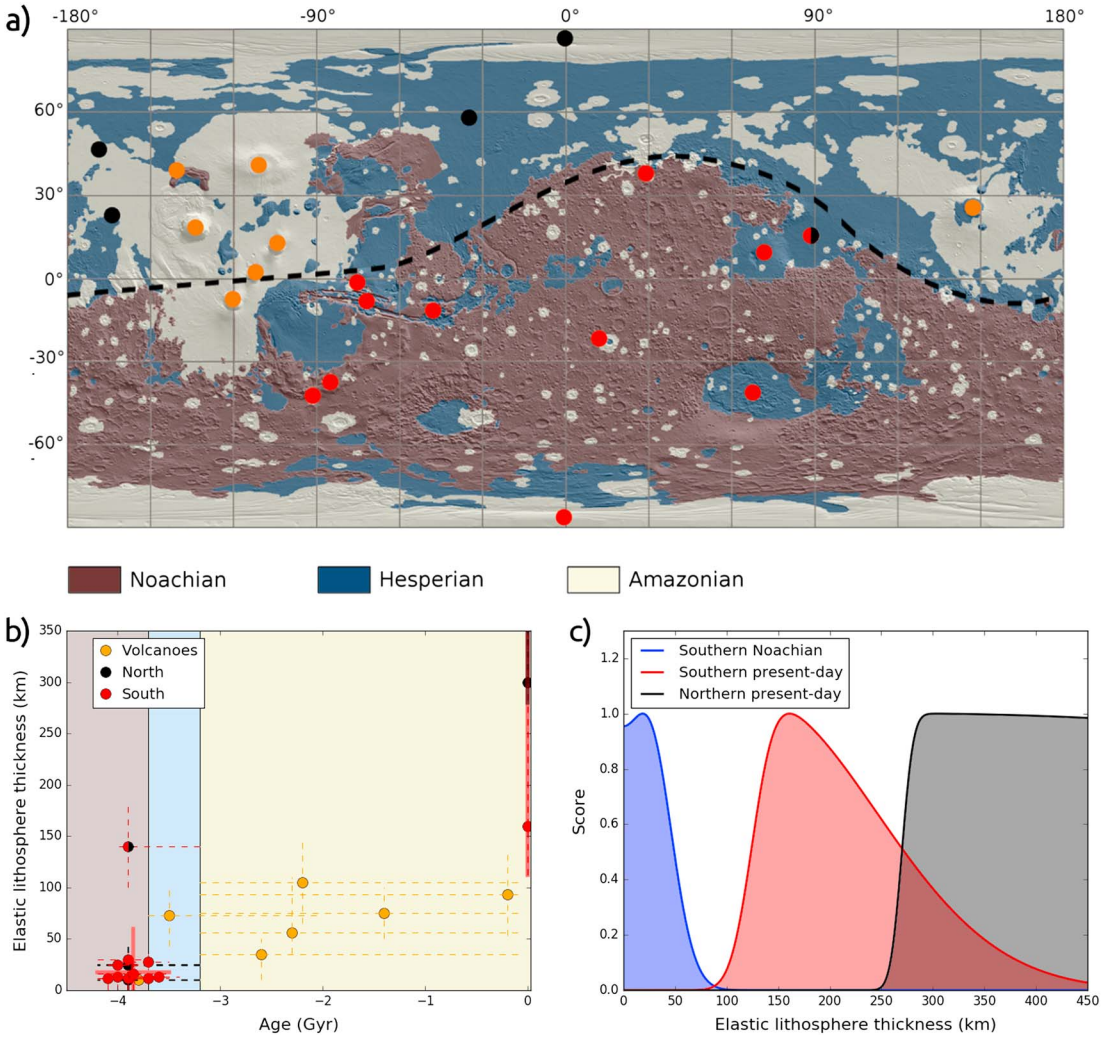

Figure 2. Constraints on elastic lithosphere thickness (T_e). (a) Location of T_e estimates, previously compiled by Grott et al. (2013), over a Mars Orbiter Laser Altimeter-shaded topographic map. The major Martian geological epochs are taken from the chronostratigraphic map of Tanaka et al. (2014). The north/south dichotomy of Andrews-Hanna et al. (2008) is shown with a dashed line. In this study we make the distinction between southern and northern values: red points are localized in the highlands, black ones in the lowlands. The orange points correspond to estimations below the large volcanoes situated close to the dichotomy. (b) T_e estimates represented on (a) are here plotted as a function of age. Errorbars are represented in dashed line for each estimate. Bold lines correspond to the three major T_e constraints considered: in the Noachian in the south and at the present day below the two polar caps. (c) Scores given as a function of the computed value of the elastic lithosphere thickness. Asymetric Gaussian distributions are used for the constraints in the Noachian south (blue), at the present day below the south polar cap (red) and below the northern one (black).

at this location could be influenced by the properties of both hemispheres but are more representative of the larger values of the north (Plesa et al., 2016). Given this wide range of values, we do not include any constraint in the Noachian in the north. We will see indeed that our results cover a large range of potential T_e in the north during this period (see section 4.1).

Elastic thicknesses have also been evaluated below large volcanoes. However, although a large fraction of these edifices, for example, Tharsis and Elysium, has probably been emplaced during the Noachian, their construction lasted several gigayears. Recent lava flows have indeed been detected on the slopes of Tharsis and Elysium (Hartmann et al., 1999; Hauber et al., 2011; Neukum et al., 2004; Susko et al., 2017; Werner, 2009), introducing a large error bar for the ages of these estimates (~3 Gyr). In addition, Tharsis is located close to the dichotomy boundary (Andrews-Hanna et al., 2008; Neumann et al., 2004). In this study, we therefore do not account for T_e estimates below large volcanoes. We rather consider present-day estimates obtained under the two polar caps as their age is well constrained. A mean value of 161 km has been obtained below the south polar cap, although any value greater than 110 km could fit the observations (Wieczorek, 2008).

Below the north polar cap, Phillips et al. (2008) have obtained values larger than 300 km. We notice that Phillips et al. (2008) have estimated a lower bound of 275–300 km for the elastic thickness below the south polar cap noting that this value could reflect the substrate topography noise. Thus, we use the less severe restriction of $T_e > 110$ km by Wieczorek (2008) (Figure 2b).

We use Monte Carlo simulations to select suitable thermal models, defined in terms of the northern and southern crustal thermal properties (see section 3.3), that are compatible with these three constraints on elastic lithosphere thicknesses (i.e., low T_e in the Noachian, present-day T_e values larger than 300 km for the north and higher than 110 km for the south).

To assess the likelihood of each model, scores on our constraints are defined. Suitable southern Noachian values are between 0 and 50 km with a best fit at 22 km. We choose an asymmetric Gaussian probability law representative of this distribution (Figure 2c) at an age of 3.85 Gyr (the mean age of Noachian estimates), normalized between 0 and 1 point. We use another asymmetric Gaussian score for the constraint on the present-day southern elastic thickness, with a maximum of 1 point at 161 km (Figure 2c). Concerning the elastic thickness constraint in the northern hemisphere, we assign the maximal score of 1 for a model that predicts $T_e \geq 300$ km in the lowlands (Phillips et al., 2008). Nevertheless, this estimate is perhaps not valid for the entire hemisphere. In 3-D thermal models, lateral variations in T_e of 20 km and 30–40 km could be observed in the lowlands with and without present-day mantle plumes, respectively (Plesa et al., 2016): we thus choose a Gaussian shape representative of this uncertainty (Figure 2c). We assume the same weight for the three constraints on T_e, which implies a maximal total score of 3 for a model.

3. Method and Modeling

3.1. Thermal Model

We adopt the 1-D parameterized model of stagnant lid convection of Grott and Breuer (2008) and consider distinct crustal properties for the two hemispheres of Mars. One-dimensional parameterized convection models are based on scaling relationships between heat flux through boundary layers and the Rayleigh number, which describes the vigor of convection (Grasset & Parmentier, 1998):

$$Ra^{\mathrm{N/S}}(T) = \frac{\alpha \rho_m g \Delta T (R_l^{\mathrm{N/S}} - R_c)^3}{\kappa \eta(T)} \tag{1}$$

where α is the coefficient of thermal expansion, ρ_m mantle density, g gravity, κ mantle thermal diffusivity, R_c core radius and ΔT the temperature difference across the boundary layers. The subscript N/S indicates that a parameter differs between the northern and southern hemispheres. In our model, we observe a north/south difference in the Rayleigh number as the lithosphere thickness and thus the radius of the mantle-lithosphere boundary $R_l^{N/S}$ are different between the lowlands and the highlands. The mantle viscosity η strongly depends on temperature which leads to the formation of a rigid lid at the surface that does not participate to the convection, the so-called stagnant lid. We use an Arrhenius law to describe the viscosity as a function of temperature and pressure:

$$\eta(T,P) = \eta_0 \exp\left(\frac{A+PV}{RT} - \frac{A+P_{\mathrm{ref}}V}{RT_{\mathrm{ref}}}\right) \tag{2}$$

where A and V are the activation energy and volume, respectively, for a linear rheology; R is the gas constant, η_0 the reference viscosity at a reference temperature $T_{\mathrm{ref}} = 1{,}600$ K and a reference pressure $P_{\mathrm{ref}} = 3 \times 10^9$ Pa.

Besides temperature and pressure, the viscosity depends on mantle water content (Mei & Kohlstedt, 2000a, 2000b) and deformation mechanism. Geochemical analysis of SNC meteorites suggests that the mantle may contain large amounts of water (McSween et al., 2001; Médard & Grove, 2006). Grott and Breuer (2008) also found that the small T_e observed during the Noachian period are in good agreement with a wet mantle rheology. However, there is no indication that water has been retained in the mantle during accretion; in addition, water could have been lost since then by dehydration due to mantle melting. We therefore consider both cases in our simulations using a reference viscosity of 10^{21} Pa s at a reference temperature T_{ref} of 1,600 K for a dry mantle rheology, and 10^{19} Pa s for a wet rheology (Karato & Wu, 1993). We also consider wet and dry rheologies for the crust.

Viscosity also depends on the deformation mechanisms at play in the mantle. On Earth, dislocation creep is predicted to dominate in the upper mantle, whereas diffusion creep is the major deformation mechanism

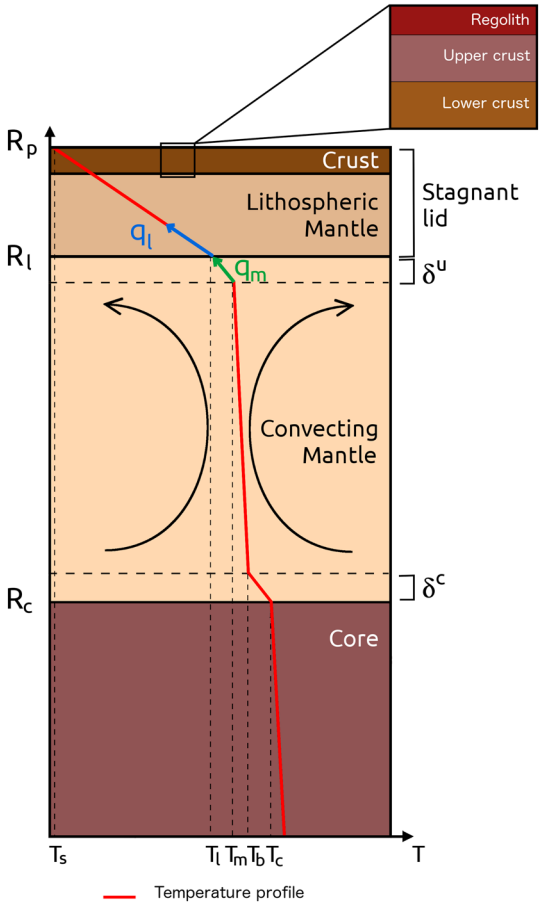

Figure 3. Sketch of the thermal parameterized model used in this study (not to scale). A phenomenological temperature profile is indicated in red. Lithosphere growth results from the difference between q_m, the heat flux out of the convecting mantle to the base of the stagnant lid, and q_l the heat which is conducted away toward the surface by conduction through the stagnant lid. The heat flux q_l is computed considering a time-dependent conduction (equation (14)).

in the lower mantle (Karato & Wu, 1993). Nevertheless, the exact style of deformation depends on grain size, which is poorly constrained in planetary mantles. Therefore, even if on Mars the gravity is lower than on Earth leading to lower pressures in the Martian mantle, diffusion creep could still be the dominant deformation mechanism. We use representative values of the linear diffusion rheology in viscosity computation (equation (2)) with $A = 300$ kJ/mol and $V = 6$ cm^3 in the case of a dry mantle rheology, and $A = 240$ kJ/mol and $V = 5$ cm^3 in the case of a wet mantle rheology (Karato & Wu, 1993). We also test the effect of dislocation creep by assuming an activation volume of $V = 7$ cm^3 and lower activation energies of $A = 200$ kJ/ mol (dry mantle rheology) or $A = 157$ kJ/mol (wet mantle rheology) in the simplified Newtonian viscosity law (equation (2)), which results from the dislocation creep activation energy and volume being divided by the stress exponent n in order to produce an equivalent temperature dependence (Christensen, 1983).

The Martian mantle is heated both internally through the decay of radioelements and from below by the core. The mantle heat balance is thus determined by the internal heating and the heat flow across the two conductive boundary layers situated at the bottom and below the surface stagnant lid, which rapidly forms due to the strong temperature dependence of the viscosity. In the mantle (excluding the boundary layers), the temperature gradient is assumed adiabatic (see Figure 3 for a sketch of the model and Table 1 for the parameters). The boundary layer theory suggests that the thickness of the boundary layers evolves as

$$\delta^{u,c} = (R_l^{N/S} - R_c)\left(\frac{Ra^{u,c}_{crit}}{Ra^{u,c}(T_m)}\right)^{\beta} \quad (3)$$

where we use $\beta = 1/3$ (Turcotte & Schubert, 2002) and the subscript u, c denotes the upper boundary layer or core-mantle boundary layer. In Ra^u we use $\Delta T^u = T_m - T_l + T_c - T_b$-where T_l is the temperature at the base of the stagnant lid, T_m the temperature at the top of the convecting mantle, T_c the temperature at the core-mantle boundary (CMB) and T_b the temperature at the base of the convecting mantle (see Figure 3)—the surface gravity g, the viscosity at the temperature T_m, and the pressure at the base of the upper thermal boundary layer. Note that $\Delta T^u = T_m - T_l$ if $T_b > T_c$, which arises when the mantle heats the core during thermal evolution. In this case the temperature difference between T_b and T_c becomes negative and does not contribute to convection anymore. In Ra^c we use $\Delta T^c = T_c - T_b$ (Figure 3), the gravity at the CMB g_c, a viscosity at the temperature $(T_c + T_b)/2$ (Richter, 1978), and the pressure at the top of the lower thermal boundary layer. $Ra^{u,c}_{crit}$ is the critical Rayleigh number at which this layer destabilizes. For the upper boundary layer we use $Ra^u_{crit} = 450$ while, for the lower boundary layer we use the local description of Deschamps and Sotin (2000) that depends on Ra^u:

$$Ra^c_{crit} = 0.28(Ra^u)^{0.21} \quad (4)$$

Starting from an initial temperature profile in the planet, which requires an assumption on the initial mantle and core temperatures, the thermal evolution of the planet up to the present day is computed by solving the energy balance equations for the core, the mantle, and the stagnant lid. Assuming that the core is well mixed and that the temperature difference across the thermal boundary layer on the core side of the CMB is negligible, energy conservation in the core can be computed as follows (Ke & Solomatov, 2009):

$$\rho_c C_c V_c \epsilon_c \frac{dT_c}{dt} = -q_c A_c \quad (5)$$

Table 1
Model Parameters

Parameter	Notation	Value	Unit
Mean planetary radius	R_p	$3,390 \times 10^3$	m
Core radius	R_c	$1,700 \times 10^3$	m
Regolith thickness	d_r	10	m
North-south mean altitude difference	dh	6×10^3	m
Northern hemisphere surface fraction	F^n	$0.3 - 0.4$	
Mantle density	ρ_m	3,500	kg/m^3
Core density	ρ_c	7,200	kg/m^3
Regolith thermal conductivity	k_r	0.1	W $\cdot$ m^1 $\cdot$ K^1
Mantle thermal conductivity	k_m	4	W $\cdot$ m^{-1} $\cdot$ K^{-1}
Surface temperature	T_s	220	K
Reference temperature	T_{ref}	1,600	K
Initial mantle temperature	T_{m_0}	1,800	K
Initial core temperature	T_{c_0}	2,050	K
Critical Rayleigh number	Ra^u_{crit}	450	
Mantle heat capacity	C_m	1,142	J $\cdot$ kg^{-1} $\cdot$ K^{-1}
Core heat capacity	C_c	840	J $\cdot$ kg^{-1} $\cdot$ K^{-1}
Ratio of the mean and upper core temperature	ϵ_c	1.1	
Surface gravity	g	3.7	m/s^2
Core-mantle boundary gravity	g_c	3.4	m/s^2
Gas constant	R	8.3144	J $\cdot$ K^{-1} $\cdot$ mol^{-1}
Thermal expansion coefficient	α	2.5×10^{-5}	K^{-1}
Activation energy	A	$1.5-3 \times 10^5$	J/mol
Activation volume	V	5–7	cm^3/mol
Reference pressure	p_{ref}	3×10^9	Pa
Strain rate (convection)	$\dot{\epsilon}$	10^{-17}	s^{-1}
Strain rate (glacial loading)	$\dot{\epsilon}_{\text{cap}}$	10^{-14}	s^{-1}
Impact temperature increase	ΔT_i	100	K

where A_c, ρ_c, C_c and V_c are respectively the surface area, the density, the heat capacity and the volume of the core, t is time, $\epsilon_c \sim 1.1$ is the ratio between the average core temperature and the temperature at the core-mantle boundary T_c (Stevenson et al., 1983). The heat flux out of the core and into the mantle q_c is calculated from:

$$q_c = k_m \frac{T_c - T_b}{\delta^c} \tag{6}$$

where δ^c is the lower boundary layer thickness and k_m the mantle thermal conductivity. The temperature at the base of the convecting mantle, T_b, is calculated from T_m and the adiabatic temperature gradient in the mantle:

$$T_b = T_m + \frac{\alpha g T_m}{C_m}(R_l - R_c - \delta^u - \delta^c) \tag{7}$$

In parallel, the mantle concedes heat to the stagnant lid with a heat flux q_m; its energy balance is thus given by:

$$\rho_m C_m V_m \epsilon_m \frac{\mathrm{d}T_m}{\mathrm{d}t} = q_c A_c - q_m A_m + Q_m V_m \tag{8}$$

with C_m the heat capacity of the mantle, Q_m the mantle heat production rate. ϵ_m is the ratio between the mean temperature of the convecting mantle and T_m, and is computed at each time step. The volume of the convecting mantle V_m is computed from

$$V_m = \frac{4}{3}\pi \sum_{\mathrm{N/S}} F^{\mathrm{N/S}}(R_l^{\mathrm{N/S}^3} - R_c^3) \tag{9}$$

with $F^{\mathrm{N/S}}$ the surface fractions of the north and south, which are 42% and 58%, respectively, if considering the dichotomy boundary of Andrews-Hanna et al. (2008), where Tharsis is located in the north (see Figure 2a). Nevertheless, the crust under large volcanoes is particularly thick and thus more similar to the southern crust of our model. We therefore vary the southern surface fraction between 60% (our reference model) and 70%. The total surface area A_m at the lid-mantle boundary is given by

$$A_m = 4\pi \sum_{\mathrm{N/S}} F^{\mathrm{N/S}} R_l^{\mathrm{N/S}^2} \tag{10}$$

The heat flux q_m out of the mantle and into the base of the stagnant lid is computed from

$$q_m = k_m \frac{T_m - T_l}{\delta u} \tag{11}$$

The base of the stagnant lid is defined by its temperature T_l, which depends on mantle temperature T_m and on the rate of viscosity change with temperature (Davaille & Jaupart, 1993):

$$T_l = T_m - 2.21 \frac{\eta(T_m)}{\mathrm{d}\eta/\mathrm{d}T|_{T_m}} = T_m - 2.21 \frac{RT_m^2}{A} \tag{12}$$

The rate of stagnant lid growth is determined by an energy balance at the base of the lid, that is, by the difference between q_m, the heat transferred from the convecting mantle to the base of the stagnant lid, and the heat which is conducted away toward the surface through the lid (Grott & Breuer, 2008):

$$\rho_m C_m (T_m - T_l) \frac{\mathrm{d}D_l^{\mathrm{N/S}}}{\mathrm{d}t} = -q_m - k_m \left.\frac{\partial T^{\mathrm{N/S}}}{\partial r}\right|_{r=R_l^{\mathrm{N/S}}} \tag{13}$$

where $D_l^{\mathrm{N/S}}$ is the stagnant lid thickness, $T^{\mathrm{N/S}}$ is the temperature in the lid and r the radial distance from the planet center. Contrary to Grott and Breuer (2008), we consider time-dependent rather than steady state heat conduction in the lid, which is more appropriate for a thick lithosphere (Michaut & Jaupart, 2004):

$$\rho_j^{\mathrm{N/S}} C_j \frac{\partial T^{\mathrm{N/S}}}{\partial t} = \frac{1}{r^2}\frac{\partial}{\partial r}\left(r^2 k_j^{\mathrm{N/S}} \frac{\partial T^{\mathrm{N/S}}}{\partial r}\right) + Q_j^{\mathrm{N/S}} \tag{14}$$

In our model, we assume that the whole mantle is well mixed. In particular, the heat flow out of the mantle, q_m, and the temperature at the base of the lid, T_l, are the same in both hemispheres, which is reasonable in the absence of large mantle plumes (Plesa et al., 2016). Nevertheless, the rate of stagnant lid growth and the temperature profile are expected to differ between both hemispheres, as they depend on crustal properties (thermal conductivity, crustal thickness, and enrichment factor) that vary between the north and south. $Q_j^{\mathrm{N/S}}$, $\rho_j^{\mathrm{N/S}}$, and $k_j^{\mathrm{N/S}}$ represent, respectively, the volumetric heat production rate, the density, and the thermal conductivity in the j different layers of the stagnant lid, that is, the regolith, upper crust, lower crust, and lithospheric mantle (Figure 3). The distinct crustal layers of volume $V_{\mathrm{cr}_j}^{\mathrm{N/S}}$, can show distinct radioelement enrichment $\Lambda_j^{\mathrm{N/S}}$ with respect to the primitive mantle. Heat production is thus computed from

$$Q_{\mathrm{cr}_j}^{\mathrm{N/S}} = \sum_i Q_i \exp(-\lambda_i t) \frac{M_{\mathrm{silicate}}}{V_{\mathrm{silicate}}} \Lambda_j^{\mathrm{N/S}} \tag{15}$$

where the sum extends over the four radiogenic species—^{40}K, ^{232}Th, ^{235}U, and ^{238}U—which have a heat production rate Q_i decreasing with time, depending on their respective decay constants λ_i. M_{silicate} and V_{silicate} are the mass and volume of the silicate bulk. Mantle heat production Q_m is then computed from mass balance.

A Runge-Kutta numerical scheme of order 4 is used to solve the ordinary differential equations (5), (8), and (13). Equation (14) is solved using an implicit numerical scheme and a change of variable $r = R_P^{\mathrm{N/S}} - D_l^{\mathrm{N/S}} y$, which allows to keep a fixed number of grid points between two fixed boundaries $y = 0$ and $y = 1$, and to adapt the grid distance according to the stagnant lid thickness that varies at each iteration. Note that the planetary radius differs between the two hemispheres with an average value of 3,390 km and a north/south altitude difference dh = 6 km.

Table 2
Rheological Parameters

Rheology	B (Pa^{-n} s^{-1})	A_n (kJ mol^{-1})	n [K]	Reference viscosity η_0 (Pa s)
Dry olivine	2.4×10^{-16}	540	3.5	10^{21}
Wet olivine	3.9×10^{-15}	430	3.0	10^{19}
Dry diabase	1.1×10^{-26}	488	4.7	-
Wet diabase	3.1×10^{-20}	276	3.05	-

Note. The parameters characterizing the rheology of dry and wet olivine for dislocation creep are those of Karato and Wu (1993). For the crust, parameters characterizing the rheology of dry diabase are from Mackwell et al. (1998) and of wet diabase from Caristan (1982).

3.2. Elastic Thickness Computation

Given the temperature structure and the rheology of the lithosphere, ductile and brittle deformation envelopes can be retrieved. By determining which deformation mechanism dominates at a given depth, it is then possible to build the strength envelope (McNutt et al., 1988).

The brittle deformation σ_B —or frictional sliding—is related to the effective vertical stress σ_v, or lithostatic pressure (Mueller & Phillips, 1995). It is essentially independent of temperature, strain rate, and in most cases, rock composition (Byerlee, 1978). It occurs as soon as a stress in extension exceeds

$$\sigma_B = \begin{cases} 0.786\sigma_v & \text{if } \sigma_v \leq 529.9 \text{ MPa} \\ 56.7 \text{ MPa} + 0.679\sigma_v & \text{if } \sigma_v > 529.9 \text{ MPa} \end{cases} \tag{16}$$

or when a compressive stress becomes greater than

$$\sigma_B = \begin{cases} -3.68\sigma_v & \text{if } \sigma_v \leq 113.2 \text{ MPa} \\ -176.6 \text{ MPa} - 2.12\sigma_v & \text{if } \sigma_v > 113.2 \text{ MPa} \end{cases} \tag{17}$$

In the lower hot lithosphere, yield strength is limited by intracrystalline ductile creep σ_D. Unlike brittle deformation it depends on the temperature profile $T(r)$ in the lithosphere, the strain rate $\dot{\epsilon}$ and lithospheric rheological parameters like the stress exponent n, the prefactor B, and the activation energy A_n for a nonlinear rheology (Durham & Goetze, 1977a, 1977b)

$$\sigma_D = \left(\frac{\dot{\epsilon}}{B}\right)^{\frac{1}{n}} e^{A_n/nRT} \tag{18}$$

The choice of these parameters is therefore crucial to determine an elastic thickness. We use rheological parameters suitable for wet and dry olivine rheology in the mantle (Karato & Wu, 1993), and wet (Caristan, 1982) and dry diabase (Mackwell et al., 1998) in the crust (see Table 2). The strain rate $\dot{\epsilon}$ in the lithosphere is usually due to underlying convection. Since Mars convection is less vigorous than on Earth, the strain rate is assumed to be low, with a value of $\sim 10^{-17}$ s^{-1} (McGovern et al., 2004). However, Martian polar caps have been emplaced a few million years ago and the strain rate at those latitudes is related to the timescale of obliquity changes that are believed to have driven the ice cap deposition (Laskar et al., 2004). We thus consider a strain rate of 10^{-14} s^{-1}, which allows a direct comparison between our present-day elastic thickness estimations and those of Phillips et al. (2008) and Wieczorek (2008) below the two polar caps. Note that this high strain rate only applies below the polar caps at the present-day, but not to the entire hemisphere, which implies different present-day estimations according to the location. In order to determine elastic lithosphere thickness from its strength envelope, one needs to evaluate the stress undergone by the lithosphere, induced by mantle convection, that is, the bounding stress σ_y. This is a decisive parameter as it sets the temperature at which ductile failure occurs, and hence the thickness of the elastic lithosphere

$$T(\sigma_y) = \frac{A_n}{R}\left[\ln\left(\frac{\sigma_y^n B}{\dot{\epsilon}}\right)\right]^{-1} \tag{19}$$

In this study, we assume a bounding stress of 15 MPa as in Burov and Diament (1995).

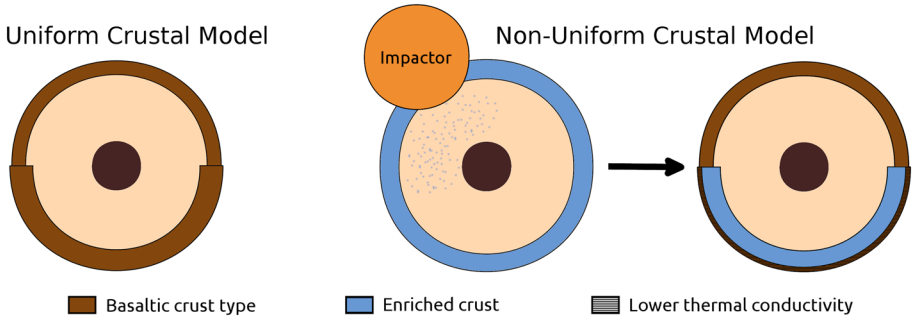

Figure 4. Sketches of the two different crustal models (not to scale). (left) In the Uniform Crustal Model the northern and southern crusts have the same properties (thermal conductivity, enrichment in radioelements, and density) but the southern one is thicker by Airy isostatic compensation of the 6 km north/south difference in altitudes. (right) In the Non-Uniform Crustal Model, the two crusts are the same initially. After a large impact remixes the northern primary crust in the mantle at 4.5–4 Gyr, a new secondary crust forms instantaneously in the north with distinct properties (composition, enrichment in radioelements, and thickness). In this crustal model the impact injects energy in the mantle as well as the additional radioelements of the primary northern crust, which triggers the formation of an upper layer of 10 km in the south with a composition similar to the northern secondary crust. This thin upper layer in the south can have a different thermal conductivity as proposed by Bandfield et al. (2013).

The rheologies differ between the crust and the lithospheric mantle: their elastic thicknesses, respectively $T_{e,c}$ and $T_{e,m}$, have therefore to be computed separately. We assume a nonflexed plate, with zero bending moment. In this way the modeled T_e could directly be compared to estimations made under the present-day polar caps or during the Noachian, for which a nonflexed lithosphere is a good approximation. Depending on the rheology and the temperature profile, $T_{e,c}$ and $T_{e,m}$ could be welded and the elastic thickness T_e is given by

$$T_e = T_{e,c} + T_{e,m} \tag{20}$$

or separated by an incompetent crustal layer, in which case T_e is given by

$$T_e = (T_{e,c}^3 + T_{e,m}^3)^{\frac{1}{3}} \tag{21}$$

3.3. Crustal Models and Parameters

According to the recent discoveries related to crustal properties (Figure 1) that could potentially mark differences in composition between the two hemispheres of Mars, we consider two different crustal models (Figure 4): one—referred to as the Non-Uniform Crustal Model (NUCM)—accounting for north/south differences in crustal properties, and a more traditional one, referred to as the Uniform Crustal Model (UCM). The latter model is defined by no north/south differences in crustal properties: both crusts have the same density and thermal parameters; but there is a hemispheric difference in crustal thickness. In particular, an Airy isostatic compensation of the 6 km difference in altitude between the two hemispheres induces a thick southern crustal root whose thickness depends on crustal density and northern crustal thickness. For the NUCM case, the northern and southern primary crusts are first assumed to be the same, resulting, for instance, from the crystallization of the primordial magma ocean and subsequent early evolution of Mars (Elkins-Tanton et al., 2003, 2005). The dichotomy formation is then modeled by an instantaneous removal of the entire primary northern crust due to a large impact and the resetting of the lithosphere thickness to that of the new northern secondary crust formed after this event. Compared to the primary crust, this secondary one is assumed to be more mafic with a higher density along with a lower radioelement content due to the depletion of the parent mantle compared to the primitive one. The radioelements of the primary northern crust as well as the energy of the impact are injected in the well-mixed mantle. The energy released by the impact into the mantle is challenging to estimate. Marinova et al. (2008) have evaluated an impact energy of 3 to 6 $\times$ 10^{29} J, one third of it being estimated to contribute to a dramatic local heating at the impact side (K. Wünnemann, personal communication, 2017). A large part of the impact energy is also consumed by melting and the formation of a new crust, limiting the temperature increase to a couple of hundred kelvins. Temperature anomalies in the north may persist for >100 Myr (Roberts & Arkani-Hamed, 2014), while the southern hemisphere is not immediatly heated (Arkani-Hamed & Olson, 2010). Nevertheless, the temperature increase is later homogenized by convection. Here we assume a simplified scenario in which the temperature

Table 3
A Priori Range of Crustal Parameters Considered in Each Hemisphere for the Two Crustal Models

	UCM	NUCM
Northern crust		
d^N (km)	30–60	30–60
ρ^N (kg/m^3)	2,900–3,200	3,100
k^N (W m^{-1} K^{-1})	3	3
Λ^N	5–15	10 or 5–15 (Appendix A)
Southern crust		
d_1^S (km)	0	10
d^S (km)	65–127	39–112
ρ_1^S (kg/m^3)	2,900–3,200	3,100
ρ_2^S (kg/m^3)	2,900–3,200	2,500–3,100
k_1^S (W · m^{-1} · K^{-1})	3	2 – 3
k_2^S (W · m^{-1} · K^{-1})	3	3
Λ_1^S	5–15	10 or 5–15 (Appendix A)
Λ_2^S	5–15	5–30

Note. For the southern crust, the index 1 corresponds to the upper layer of 10 km ($= d_1^S$) and $j = 2$ to the lower one whose thickness is $d_2^S = d^S - d_1^S$. The subscript N/S relates to the northern or southern hemisphere, respectively; d is the thickness, ρ the density, k the thermal conductivity, and Λ the enrichment factor in radioelements with respect to the primitive mantle.

rises by ~100–200 K in the entire mantle following the impact. We also suppose that the injection of radioelements and impact energy into the mantle results in the production of high flows of hot and buoyant basaltic melt that could, as observed on Earth, reach the southern surface and form an upper thin crustal layer in the south, of the same type as that in the north. This would explain the absence of a large difference in surface composition between hemispheres. We thus assume the instantaneous formation of a surficial crustal layer in the south of the same composition as the secondary northern crust, but with a thermal conductivity that can be lower, consistent with porous materials formed by pyroclastic volcanism (Bandfield et al., 2013). In both crustal models, we do not account for crustal formation by mantle partial melting. As the bulk of the crust is supposed to have formed within the first gigayears of evolution (Grott, 2005; Hartmann & Malin, 2000, 1999; Hauber et al., 2009; Werner, 2009), we do not expect that this would have a strong effect on our results, especially at the present day. Nevertheless, we range the age of the dichotomy formation between 4.5 and 4 Gyr, and choose 4.4 Gyr in our nominal model.

Constraints on crustal thickness are mainly derived from topography and gravimetry data (Neumann et al., 2004; Wieczorek & Zuber, 2004; Zuber et al., 2000), or from the absence of large-scale relaxation of the topography (Nimmo & Stevenson, 2001). Assuming a uniform crustal density of 2,900 kg/m^3, Neumann et al. (2004) retrieved average crustal thicknesses of 32 and 58 km in the lowlands and highlands, respectively. Nevertheless, other crustal models considering higher crustal densities up to 3,200 kg/m^3 found thicker crusts both in the north and in the south (with averages as high as 60 and 110 km, respectively) that could fit the topography and gravity data (Plesa et al., 2016; Wieczorek & Zuber, 2004). By evaluating the global chemical composition of the Martian surface and meteorites, Baratoux et al. (2014) have reestimated crustal grain density to values higher than 3,100 kg/m^3. Assuming therefore that the 32 km of Neumann et al. (2004) is a lower bound, we use the range 30–60 km for the northern crustal thickness in our two crustal models. For the UCM simulations, we consider a basaltic crust with a density between 2,900 and 3,200 kg/m^3, whereas for the NUCM simulations we assume a density of 3,100 kg/m^3 for both the northern crust and the upper basaltic part of the southern one. The latter is assumed to have a thickness of 10 km, which is coherent with the detection of outcrops of different thermal inertia by Bandfield et al. (2013) along with the excavation depth of felsic material estimated by Carter and Poulet (2013). The density of the buried part of the southern crust is varied between 2,500 and 3,100 kg/m^3 for the NUCM simulations, representing compositions ranging from felsic to basaltic. In the two crustal models the southern crustal thickness is computed considering isostatic compensation of the higher

topography (with an average of ~6 km) of the south. Though it is not expected to have an effect on the global thermal structure and evolution, we also account for a 10 m thick regolith layer at the surface (Warner et al., 2017) that could influence the stagnant lid temperature profile. Finally, we check that all our simulations are compatible with Mars's moment of inertia (Konopliv et al., 2006).

In some models, at the beginning of the thermal evolution, the stagnant lid could become thinner than the crust, which would lead to crustal recycling. This process is favored by thick and insulating crusts, highly enriched in radioelements, that drive high crustal temperatures. Such a recycling is incompatible with the SNC geochemical characteristics (Jagoutz, 1991; Papike et al., 2009) and with the north/south isostatic equilibrium that we impose at the beginning of our simulations: we thus rule these models out.

The Martian crust is supposed to be mainly composed by compact volcanic materials. The thermal conductivity of this type of rocks is estimated between 1.5 and 3.5 $W \cdot m^{-1} \cdot K^{-1}$ at ambient conditions and decreases when temperature increases (Clauser & Huenges, 1995; Seipold, 1998). Many uncertainties remain, however, when considering real Martian conditions: the structure of crustal rocks such as their porosity and percentage of ice cement could lower the thermal conductivity (Mellon et al., 2004); a hydrothermal circulation in the upper crust could, on the contrary, significantly increase it (Parmentier & Zuber, 2007). We assume a thermal conductivity of 3 $W \cdot m^{-1} \cdot K^{-1}$ for the entire crust with the exception of the upper southern layer for the NUCM simulations where the conductivity varies between 2 and 3 $W \cdot m^{-1} \cdot K^{-1}$ to account for the poorly compacted materials pointed out by Xiao et al. (2012), Bandfield et al. (2013) and Huang and Xiao (2014) (see section 1). The thermal conductivity of the lower southern crust is supposed to be the same as that in the northern crust, as the rocks are being compacted with depth. In the fractured and poorly compacted regolith we assume a lower value of 0.1 $W \cdot m^{-1} \cdot K^{-1}$ (Gagnepain-Beyneix et al., 2006). See Table 3 for a summary of UCM and NUCM crustal parameters.

3.4. Heat Production

The choice of the bulk radioactive element content is crucial as it determines heat production and thermal evolution. While the compositional model of Wänke and Dreibus (1994) is today widely accepted, the distribution of radioelements between the crust and mantle remains unfortunately poorly constrained on Mars. The latter is a crucial parameter of our model since heat produced in the crust is easily conducted away toward the surface, while the heat produced into the mantle is harder to evacuate. Crustal radioactivity enrichment factors relative to the primitive mantle between 4 (Nimmo & Stevenson, 2001) and 10 (Grott & Breuer, 2009; Schumacher & Breuer, 2006) have been previously considered. Given gamma-ray spectroscopy (GRS) observations, Taylor et al. (2006) have suggested that about half of the bulk radioelement content is situated in the crust if an average crustal thickness of 57 km is considered, which corresponds to a crustal enrichment factor of 10. In this study, as crustal thicknesses vary over a wide range of values, we vary the crustal enrichment factor between 5 and 15 for the UCM simulations. For the NUCM simulations the enrichment factor of the northern crust and the upper part of the southern one is set equal to the average value of 10. In a second set of NUCM simulations (NUCM2, Appendix A), we also vary the northern crustal enrichment factor and consider the same range as for the UCM case, that is, 5 to 15. For the buried part of the southern crust, which may have formed very early by primary differentiation processes, we use a wider range of enrichment factors: from 5 to 30.

3.5. Initial Conditions

The initial mantle temperature T_{m_0} is largely uncertain, but it is constrained by the solidus and liquidus temperatures, which are respectively 1,600 and 2,300 K (Takahashi, 1990). Indeed an initial mantle temperature lower than the solidus is not consistent with early crustal formation. On the other hand, an initial temperature higher than the liquidus would imply a long persistence of the primordial magma ocean (Schubert & Spohn, 1990). Crustal thicknesses are also predicted to be too large if high initial temperatures, close to the liquidus, are considered (Breuer & Spohn, 2006; Hauck & Phillips, 2002; Parmentier & Zuber, 2007). Following Grott and Breuer (2009), we consider an initial mantle temperature of 1,800 K. We discuss briefly the effect of this parameter in section 5.4. The initial core temperature T_{c_0} is estimated using an adiabatic temperature increase from T_{m_0} through the mantle. We do not assume an initial superheating of the core.

4. Results

We first show in this section a sample result for a dry mantle and wet crust in association with diffusion creep, our favored rheology. Other rheologies are discussed in section 5.3 and Appendix B.

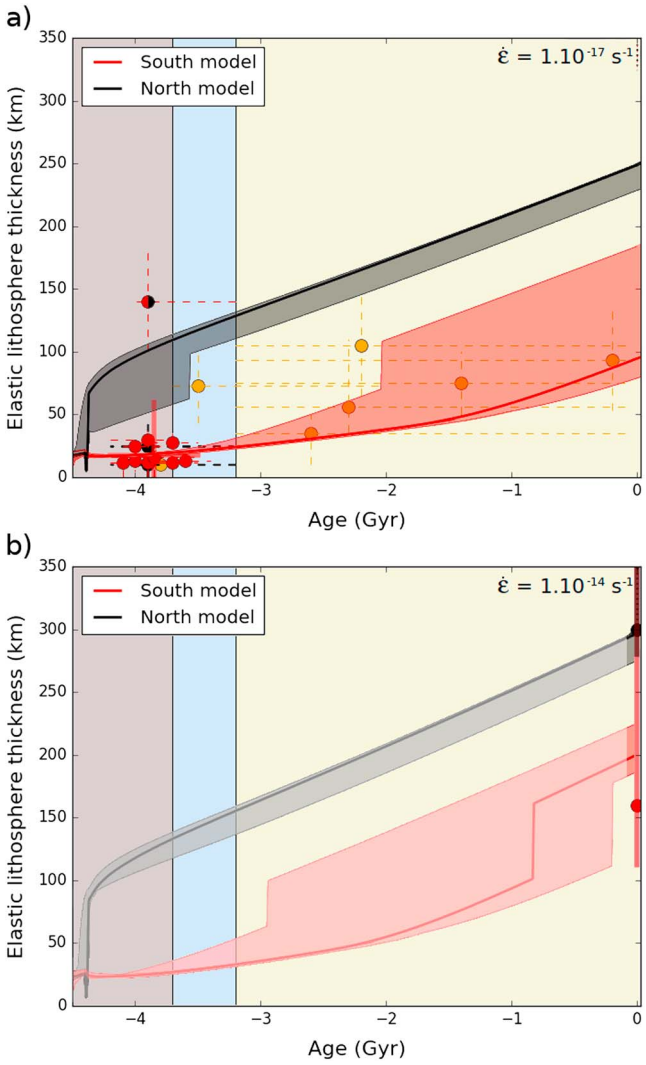

Figure 5. Elastic lithosphere thickness evolution as a function of age for the models that fit all four constraints, including present-day volcanism, in the south (red) and north (black), (a) for $\dot{\epsilon} = 10^{-17}$ s^{-1}, a strain rate representative of the time scale of mantle convection and (b) for $\dot{\epsilon} = 10^{-14}$ s^{-1} below the two polar caps, where the strain rate is representative of the timescale of polar cap deposition. Note that the elastic lithosphere thickness calculated in (b) should only be applied below the polar caps at the present day, but not to the entire hemisphere. Our reference model (Non-Uniform Crustal Model, see section 4.1 for crustal properties) is represented by bold lines, whereas shadowed areas show the range of T_e evolution that we obtain for the models showing the best scores (between 2.5 and 2.91) for both the Uniform Crustal Model and Non-Uniform Crustal Model cases.

4.1. Reference Model

We present here a reference model for the elastic lithosphere thickness evolution obtained with one of our thermal models that best fits the three constraints on elastic thickness defined in section 2 (Figures 5a and 5b, bold lines, red for the south, black for the north). This evolution corresponds to a NUCM case that considers north/south thicknesses of 32/70 km (including the upper layer thickness of 10 km in the south), enrichment factors of 10/13.1, densities of 3,100/3,003 kg/m^3, respectively, and a thermal conductivity of 2 W · m^{-1} · K^{-1} in the upper southern layer.

There is a large difference in elastic lithosphere thickness evolution between the two hemispheres. Before the dichotomy-forming impact at 4.4 Gyr, both hemispheres show a similar evolution since the crust is everywhere the same. Thereafter, north and south elastic lithosphere thicknesses diverge with very low values in the southern hemisphere that fit T_e estimates during the second part of the Noachian era (Figure 5a). The subsequent evolution is characterized by a slow increase in thickness in the south, reaching only 80 km at the present day for $\dot{\epsilon} = 10^{-17}$ s^{-1}, because, for this strain rate, an incompetent weak crustal layer is still present, decoupling the elastic upper crust from the elastic upper mantle. Nevertheless, for a higher strain rate of $\dot{\epsilon} = 10^{-14}$ s^{-1}, a value representative of cyclic ice loading, this weak layer disappears, leading to an elastic thickness equal to 193 km below the southern polar cap at the present day (Figure 5b). This is higher than the 161 km best estimate of Wieczorek (2008) but suits our southern present-day constraint (Figures 2b and 2c). In the north, after the formation of a new, thinner and more depleted secondary crust at 4.4 Gyr, the elastic lithosphere thickness quickly rises to high values of ~100 km at 3.9 Gyr, interestingly close to T_e estimates of 100–180 km at Isidis Planitia. Our model predicts higher Noachian northern elastic thicknesses than those estimated by Hoogenboom and Smrekar (2006) even though other models are close to the upper bound of these estimates (shaded areas on Figure 5a). The discontinuity at ~4.3 Gyr in T_e evolution is due to the disappearance of the incompetent crustal layer in the north, which occurs much earlier in the lowlands because of its thinner and colder crust. The Hesperian and Amazonian periods show a regular increase in T_e, more pronounced than in the southern hemisphere due to the lower radioelement content. Values of the order of 250 km for $\dot{\epsilon} = 10^{-17}$ s^{-1} are finally reached during the last stages of evolution, implying a north/south difference of 180 km in T_e (Figure 5a). Below the northern polar cap, at the present day and for $\dot{\epsilon} = 10^{-14}$ s^{-1}, the elastic thickness reaches 293 km, in good agreement with our constraint (Figure 5b).

Similarly, good fits to our three main constraints can be obtained when considering the UCM case. During the earlier stages, north/south T_e evolution curves diverge from the beginning since the crustal dichotomy is already emplaced. Shaded areas on Figures 5a and 5b represent the range of T_e evolution that we obtain from the simulations—from both the UCM and NUCM cases—that best fit T_e constraints. These models are presented in section 4.3.

4.2. Monte Carlo Simulation Results

4.2.1. Uniform Crustal Model

For the UCM case, we test the influence of three main parameters on T_e evolution: the thicknesses of the northern and southern crusts (which are closely linked to their densities), and the crustal radioactivity enrichment factor.

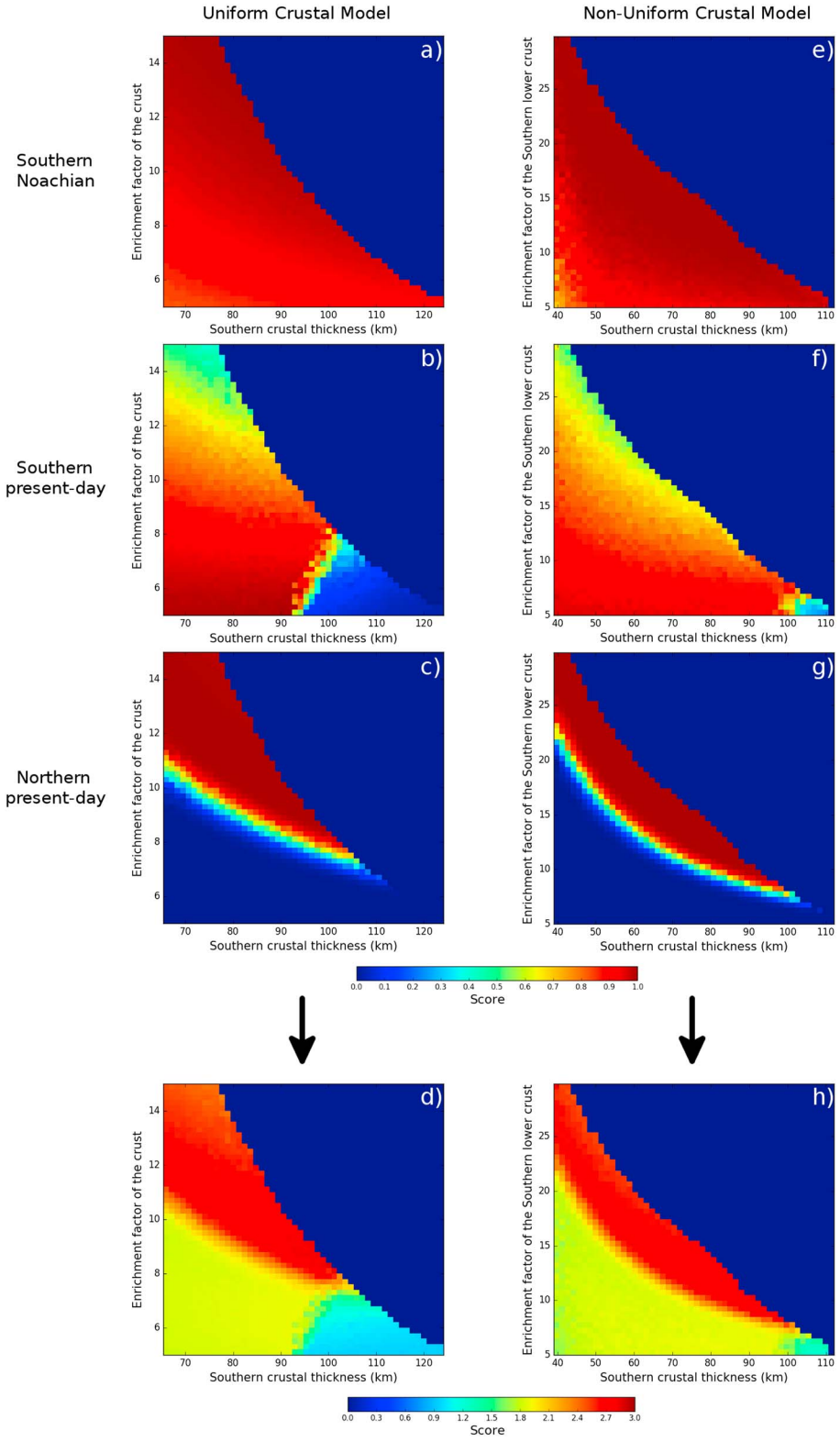

Figure 6. Results of the Monte Carlo simulations for the Uniform Crustal Model (a–d) and Non-Uniform Crustal Model (e–h) cases. Scores are represented in a color scale as a function of the southern crust thickness and radioelement enrichment factor for each T_e constraint: from top to bottom in the Noachian in the south, at the present day in the south and in the north, as well as for these three constraints altogether (d and h). See Figure 2c for score definition and main text for detailed parameter ranges.

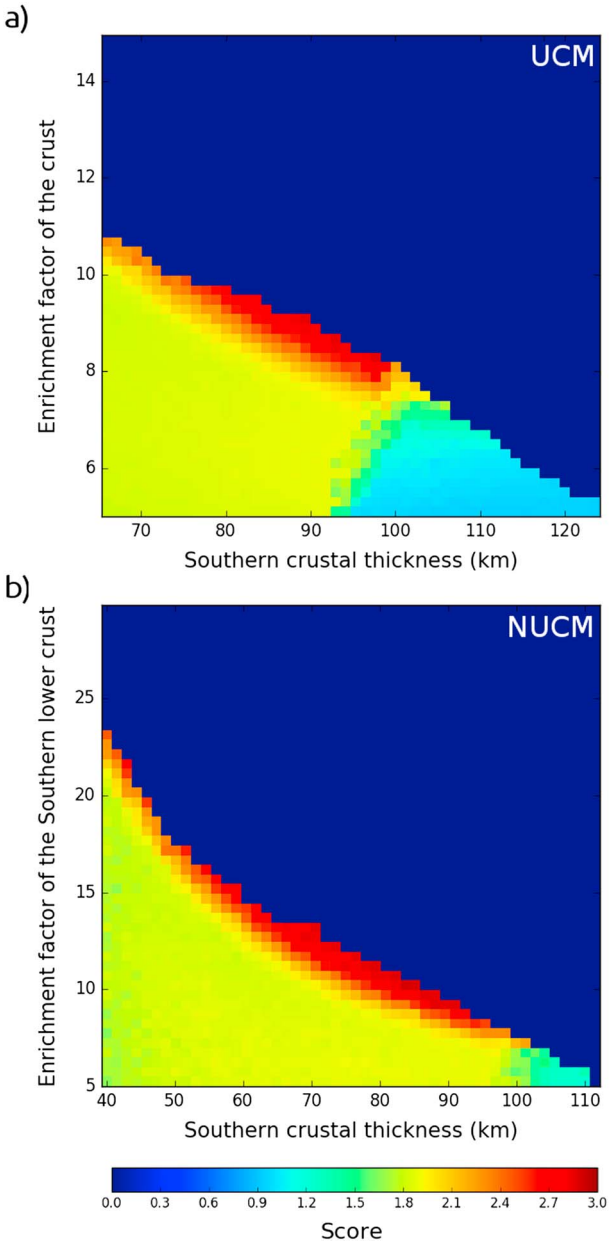

Figure 7. Results of the Monte Carlo simulations using the constraints on present-day volcanism in the south, for the Uniform Crustal Model (a) and the Non-Uniform Crustal Model (b) simulations. Scores are represented in a color scale as a function of the southern crust thickness and enrichment factor in radioelements. See Table 4 and Figure 8 for detailed parameter ranges.

As expected, the present-day value of T_e below the northern polar cap is a strong constraint, which can be fitted only when considering large crustal radioelement contents, either with thick southern crusts relatively poorly enriched compared to the primitive mantle or with thinner crusts more enriched in radioelements (Figure 6c). Suitable models for this constraint—that is, with a score >0.5—predict a southern crustal thickness of 65 to 103 km, a northern one of 30 to 58 km, a crustal density of 2,900 to 3,170 kg/m^3, and an enrichment factor between 7.6 and 14.7. The low southern Noachian elastic thicknesses are fitted with a wide range of values for all parameters and do not provide a strong constraint for crustal parameters (Figure 6a). Indeed, a wet crustal rheology implies a weak crust with an incompetent layer, at least during the early evolution, which decouples the elastic upper crust and lithospheric mantle inducing a low effective T_e in agreement with observations. We note, however, that the crustal parameters for which the best scores for the northern present-day constraint are obtained, (that is, relatively thin southern crusts and high bulk enrichment factors), deliver also the best scores for the Noachian T_e constraint. This is not the case for the present-day value of T_e below the southern polar cap (Figure 6b) for which the best fits are obtained for a similar crustal thickness but a much lower enrichment factor (bulk enrichment factor of ~5–7). This discrepancy between the crustal enrichment factor predicted by the two present-day constraints is due to the fact that if a lot of radioelements are present in the mantle, this latter is hotter and therefore allows to fit a low T_e under the southern polar cap. On the opposite, if a large amount of radioelements is concentrated in the crust, the mantle is colder and high present-day T_e could be reached in the northern hemisphere. In return, the T_e in the south are also high but still in agreement with the >110 km constraint. In general, models with a thick southern crust and a low enrichment factor are characterized by present-day values of T_e that are too low, both in the north (<280 km) and in the south (<110 km). On the contrary, models with large crustal thicknesses and strong radioelement enrichments might lead to crustal recycling, which is associated to a score equal to 0 and is responsible for the clear limit between areas with a high score and areas having a score equal to 0 (Figure 6d).

4.2.2. Non-Uniform Crustal Model

Even though we test the effect of more parameters in this crustal model—thicknesses of the two crusts, enrichment in radioelements, density of the lower southern crust layer, and thermal conductivity of the upper one—results for the NUCM case are similar in many ways to those for the UCM case: the range of parameters required to fit the southern Noachian and northern present-day constraints are in good agreement (Figures 6e and 6g), while the range of parameters required to fit the southern present-day T_e constraint predicts poorly enriched southern crusts (Figure 6f). For the NUCM simulations our best scores, that is, simulations fitting our three T_e constraints (red zone on Figure 6h), are obtained when considering a southern crustal thickness between 39 and 99 km (including the 10 km basaltic upper crust), and a southern lower crustal enrichment factor ranging from 7.8 to 29.8, while we use a value of 10 for the northern crust. The clear negative trend between the southern crustal thickness and enrichment factor, shown by models with best scores, illustrates the need to have a large amount of radioelements in the crust in order to get a cold northern hemisphere and fit the northern present-day constraint. The crustal radioelements need to be concentrated in the south, to provide low elastic thicknesses in agreement with the two constraints in the south. The southern crustal radioelement content is however limited by crustal delamination processes in the case of a thick southern crust, which is illustrated by the abrupt boundary between high score and zero score models in Figure 6h. In the case of a thin and highly enriched southern crust, this boundary is due to parameter combinations

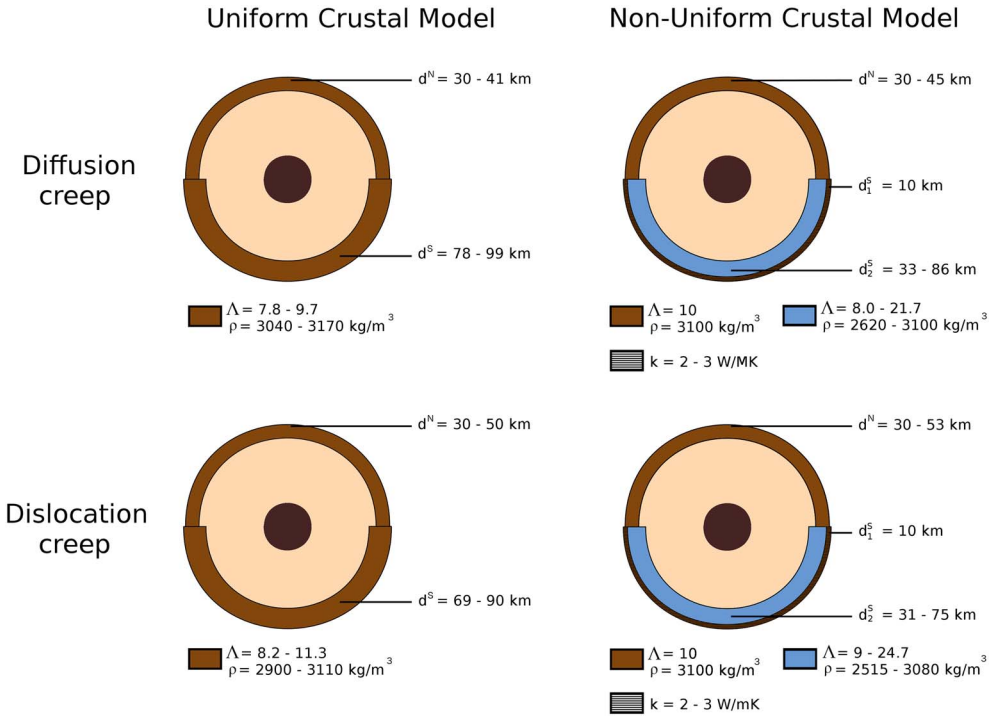

Figure 8. Summary of the crustal properties of our best models, for diffusion creep (top) and dislocation creep (bottom) rheologies.

requiring more radioelements than those actually available in the planet inventory, as, before the impact, the northern primary crust has the same characteristics as the southern one. The northern crustal thickness as well as the thermal conductivity of the southern upper crust and the density of the southern lower crust are not constrained: the entire proposed range of values are suitable. The lower southern crustal density correlates positively with the crustal thickness (the denser, the thicker) and hence negatively with the enrichment factor (the denser, the less enriched). Interestingly for the NUCM simulations, very thin southern crusts (lower than 50 km) could fit the constraints if they are very enriched in radioelements (up to 30 compared to the primitive mantle).

4.3. Accounting for Recent Volcanism

The range of suitable crustal parameters can be further constrained by Mars's volcanic activity. Recent volcanism, in the form of lava flows that might be as young as a few tens of million years, has been observed in the large volcanic complexes of Tharsis (Hartmann et al., 1999; Hauber et al., 2011; Neukum et al., 2004; Werner, 2009) and Elysium (Susko et al., 2017; Vaucher et al., 2009). This implies melt formation under Mars present-day mantle conditions, probably in mantle plumes localized under the large volcanoes (Li & Kiefer, 2007; O'Neill et al., 2007). These mantle plumes likely originate at the core-mantle boundary, with a temperature T_c characteristic of this depth. During their rise they cool adiabatically and their temperature at the depth z is given by

$$T_{\text{plume}}(z) = T_c - \frac{\alpha g T_c z}{C_m} \tag{22}$$

In order to test if current melt formation is feasible in our models, we compare the temperature profile in plumes $T_{\text{plume}}(z)$ with the solidus temperature $T_{\text{solidus}}(z)$ of a peridotite given by the parameterization of Takahashi (1990) from laboratory experiments:

$$T_{\text{solidus}}(P) = 1409 + 134.2P - 6.581P^2 + 0.1054P^3 \tag{23}$$

where P is the pressure in GPa and $P(z) = \rho(z)gz$, g is gravity and $\rho(z)$ is density, the density of the mantle is 3500 kg/m^3. Suitable models are those where melt is formed at the base of the lid beneath large volcanoes.

Table 4
Range of Crustal Parameters and Characteristics of the Present-Day Thermal Structure Predicted by the Models That Fit the Four Constraints, Including Present-Day Melt Formation in the South

	UCM	NUCM	NUCM2
Northern crustal parameters			
d^N (km)	30–41	30–45	30–55
ρ^N (kg/m^3)	3,040–3,170	3,100	3,100
k^N (W · m^{-1} · K^{-1})	3	3	3
Λ^N	7.8–9.7	10	5–13.5
Northern PBR (%)	11.1–13.8	12.7–19	6.4–20.3
Southern crustal parameters			
d_1^S (km)	0	10	10
d^S (km)	78–99	43–96	40–96
ρ_1^S (kg/m^3)	3,040–3,170	3,100	3,100
ρ_2^S (kg/m^3)	3,040–3,170	2,620–3,100	2,530–3,100
k_1^S (W · m^{-1} · K^{-1})	3	2–3	2–3
k_2^S (W · m^{-1} · K^{-1})	3	3	3
Λ_1^S	7.8–9.7	10	5–13.5
Λ_2^S	7.8–9.7	8–21.7	7.7–26.8
Southern PBR (%)	42.7–46.6	44.5–51.2	42.6–56.8
Present-day predictions			
Northern SLT (km)	443 [434–459]	445 [433–471]	445 [431–479]
Southern SLT (km)	337 [321–349]	347 [326–371]	346 [313–373]
Difference in temperature (K)	268 [229–301]	246 [170–304]	249 [168–327]
Northern SHF (mW/m^2)	17.6 [17.1–18.1]	18.2 [17.1–19.5]	17.1 [15.1–19.9]
Southern SHF (mW/m^2)	25.2 [24.8–25.6]	25.8 [25.0–26.5]	26.5 [24.6–27.8]

Note. For the NUCM2 simulations the enrichment factor of the northern crust is allowed to vary between 5 and 15 (see Appendix A). Notations are similar to those used in Table 3 and PBR corresponds to the fraction of the bulk radioelement content contained in the crust. We provide the average and range of values (in square brackets) of our predictions concerning the present-day thermal structure in the north and south, that is, the stagnant lid thickness (SLT), surface heat flux (SHF), and the north/south differences in temperature at a depth of 150 km.

These volcanoes are located in the south because such provinces have a thick crust, similar to the southern one of our model. Since large plumes penetrate and erode the stagnant lid, we allow for plume penetration in the stagnant lid over a height of 100 km, which is reasonable given present-day stagnant lid thickness range of 260–480 km. This means that we compare T_{solidus} and T_{plume} up to a depth $z = D_l^S - 100$ km in the south, where the temperatures are higher.

Models that present a rather thin southern crust strongly enriched in radioelements concentrate the heat production near the surface, which is easily conducted away: these models cool too efficiently to be compatible with present-day melt formation. For the UCM case, enrichment factors higher than 9.7 for the entire crust and southern crustal thicknesses lower than 78 km are no longer suitable (Figure 7a). For the NUCM case, the properties of the southern lower crust are also more constrained with a crustal thickness of 43–96 km (for a minimum density of 2,620 kg/m^3) and an enrichment factor limited to values <21.7 (Figure 7b). The northern crustal thickness is also constrained to values of 30–45 km for both UCM and NUCM simulations. We note, however, that taking into account the lower solidus of Kiefer et al. (2015) rather than that provided by Takahashi (1990) would make melt formation easier and thus extend the range of admissible parameters to thinner southern crusts more enriched in radioelements. Finally, we observe that none of our suitable models predicts present-day melt formation in the north, in good agreement with observations. These results are summarized in Figure 8 and Table 4.

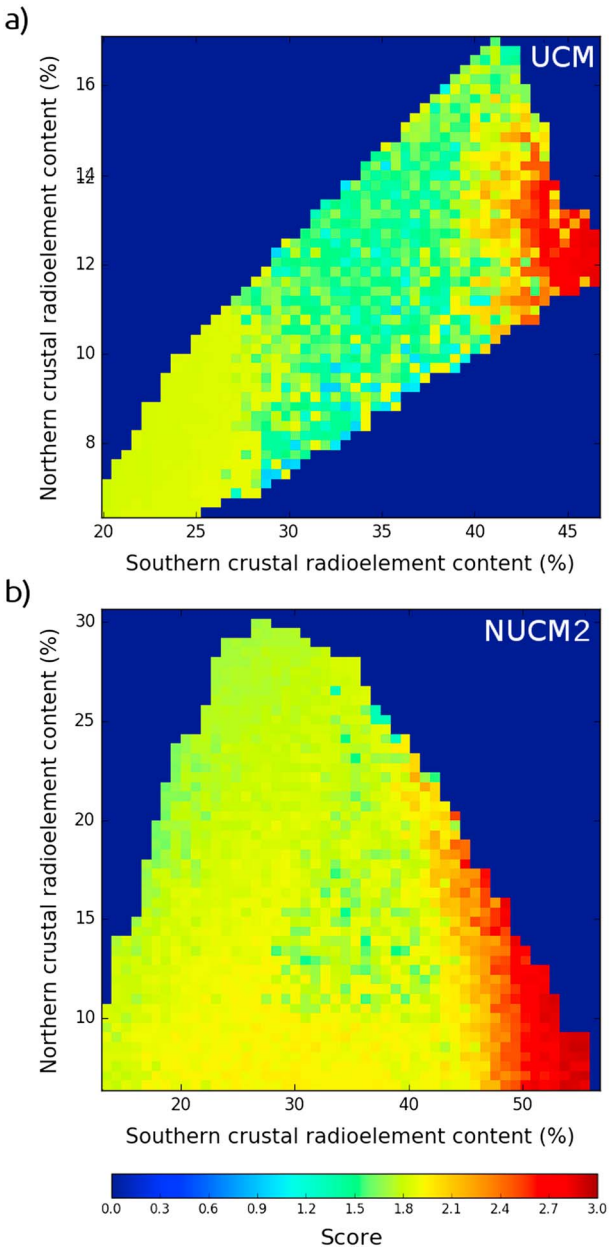

Figure 9. Results of the Monte Carlo simulations using the constraints on present-day volcanism in the south. Scores are represented in a color scale as a function of the radioelement contents of the two hemispheres, for the (a) Uniform Crustal Model and the (b) Non-Uniform Crustal Model 2 (NUCM case where we vary the northern crustal enrichment factor, see Appendix A) simulations. See Table 4 for detailed parameter ranges.

5. Discussion

The following best models refer to those that fit the three constraints on elastic thickness with a score higher than 2.5 and current melt formation in the southern hemisphere.

5.1. Model Predictions on Radioelement Concentrations

GRS measurements give surface concentrations of 2,000–6,000 ppm for K and 0.2–1 ppm for Th (Taylor et al., 2006). Using the compositional model of Wänke and Dreibus (1994), our best UCM cases predict a crustal enrichment factor of 7.8–9.7 resulting in concentrations of 2,380–2,960 ppm for K and 0.44–0.54 ppm for Th, in good agreement with GRS data. Similarly, our NUCM cases showing the best scores are in the range of GRS measurements for surface concentrations where we assume $\Lambda_N = 10$. Even though the potentially more enriched southern lower crust is buried and might not influence surface measurements, we obtain K content of 2,440–6,620 ppm and Th concentrations of 0.45–1.2 ppm for this layer, which remains in good agreement with surface data. In general, our results lie close to the upper bound of the enrichment factors usually taken for the Martian crust (Grott & Breuer, 2008, 2009; Nimmo & Stevenson, 2001; Schumacher & Breuer, 2006; Taylor et al., 2006), although they can be much higher if the north and south differ (NUCM simulations), consistent with a smaller degree of partial melting for crustal production, though still remaining in good agreement with the constraints we have on radioelement concentrations.

Our models suggest that the crust concentrates 55–65% of the bulk radioelement content of the planet, with more than 42% in the southern crust (see Figure 9 and Table 4), implying an important mantle depletion in radioelements. Since the partition coefficients of water and heat sources are similar (Morschhauser et al., 2011), a significant mantle depletion in water is also expected. Our mantle depletion is stronger than the 50% suggested by Taylor et al. (2006) although the surface concentration in radioelements is similar. This difference can be explained by the thicker average crust needed to explain the constraints of the elastic lithosphere thickness. Note that for the NUCM simulations, more radioelements (70–80%) are contained in the crust before the impact because both the northern and southern crusts have then a high radioelement content and thickness, implying a mantle even more depleted. Such a depletion could be explained by extraction of radioelements through basaltic volcanism with a low degree of partial melting or could result from initial magma ocean solidification as crystallization proceeded from the bottom up (Elkins-Tanton et al., 2003), resulting in a high concentration of incompatible radioelements near the surface. A large depletion in radioelements is necessary to retrieve very large present-day elastic lithosphere thickness in the north, whereas the low Noachian and present-day southern T_e constraints could be fitted either with a large southern crustal radioelement content or with a hot and poorly depleted mantle. Among all models, the best scores are thus obtained for the highest southern radioelement content that are feasible without crustal delamination (Figures 9a and 9b). In those models, the northern crust contains few radioelements, due to either a thin crust in both UCM and NUCM simulations, or to a low enrichment factor for the NUCM2 ones (see Appendix A).

Sekhar and King (2014) have shown that a prominent degree 2 structure of convection is observed at ~4 Gyr if a lot of heat sources (100% in their simulations) are concentrated into the crust. Such a planform of mantle convection could explain the generation of large plumes below Tharsis and Elysium Mons. Nevertheless the authors also note that present-day volcanism requires a higher content of radioelements in the mantle.

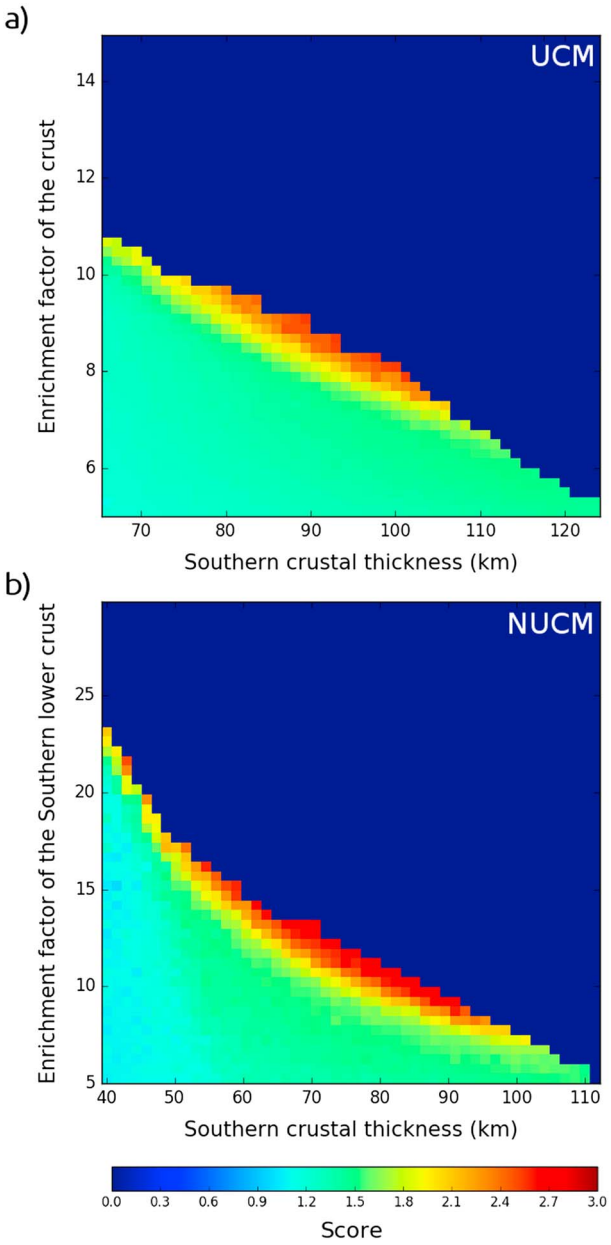

Figure 10. Results of the Monte Carlo simulations using a dry mantle and dry crustal rheology for the (a) Uniform Crustal Model and the (b) Non-Uniform Crustal Model simulations. Scores are represented in a colorscale as a function of the southern crust thickness and enrichment factor. See Appendix B for detailed parameter ranges.

Our NUCM case could represent an alternative scenario to explain this apparent paradox on crustal radioelement content. Indeed, before the impact a large part of the radioelements are contained in the crust (up to 80%): during this early stage a degree-two convection structure may have formed. As the secondary crust is less enriched in radioelements, the impact reinjects the additional radioelements of the northern primary crust into the mantle resulting in a more enriched mantle, which could explain the longstanding volcanic activity.

5.2. Crustal Thickness and Density Predictions

We find an average range of 40–75 km for the global crustal thickness, with a similar average thickness of 35 km in the north for both the UCM and NUCM simulations, whereas the estimations in the south are more scattered. In this hemisphere an average of 80 km is retrieved, but significantly thinner southern crusts cannot be ruled out as 5% of the NUCM best cases show values <60 km (see Table 4 for the total ranges). Neumann et al. (2004) obtained the same bimodal distribution of crustal thicknesses but with thickness peaks at 32 and 58 km, whereas Wieczorek and Zuber (2004) found values of 38 and 62 km. There is thus a close agreement with the values that we retrieve in the north, but not in the south where our models generally predict thicker crusts. This is due to the larger crustal densities of our best models compared to those of Neumann et al. (2004) and Wieczorek and Zuber (2004). The quite large crustal densities of most of our best models would be more compatible with estimates of Baratoux et al. (2014) for a porosity of 5–10% in the crust, but a few models that consider high radioelement enrichment factors in the south (>18) are coherent with the low-average crustal thickness value of 42 km given by Goossens et al. (2017). However, we observe that these latter models do not fit the present-day volcanism constraint if the southern surface fraction is increased to values of 65–70%.

5.3. Effect of the Mantle and Crustal Rheology

The rheology of mantle and crust has a large impact on the elastic thickness calculations and depends on the mantle and crustal water contents as well as on the deformation mechanism, which are poorly constrained. In the previous sections, we have presented results for a dry mantle and wet crustal rheology along with diffusion creep. Assuming instead a dry mantle and dry crustal rheology provides similar results to the dry mantle and wet crustal one, except that the low Noachian T_e cannot be fitted by the UCM simulations. This finding is similar to Grott and Breuer (2009) and Morschhauser et al. (2011) who argue that a wet crust is necessary to explain the low elastic thickness in the Noachian. However, for the NUCM simulations the situation is slightly different as it shows that a dry crust is compatible with the observation although values of the elastic lithosphere thicknesses in the Noachian are in the upper range of permissible values (see Appendix B and Figure 10). In addition, we find that none of our simulations with a wet olivine mantle rheology could retrieve suitable fit to our three T_e constraints (see Appendix B). In particular, the present-day north elastic thicknesses are much lower than the ≥300 km constraint. With a wet mantle rheology, Grott and Breuer (2009) could retrieve higher global T_e, close to 300 km, if they consider a large crustal radioelement content > 80%, but they use a steady state temperature profile in the stagnant lid. In fact, transient effects caused by heat transport in a thick stagnant lid should be large (Michaut & Jaupart, 2004). The time-dependency of the conductive temperature profile leads to higher temperatures in the lithosphere, inducing lower elastic thicknesses. Moreover a present-day dry mantle rheology is more consistent with the high crustal radioelement contents obtained by our best models (>55% of the bulk heat sources). Indeed, extraction of radioelements due to partial melting of the mantle and crustal formation also implies a similar extraction

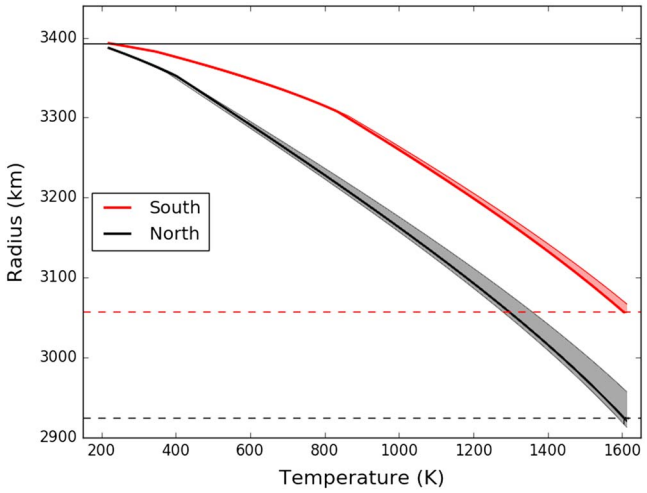

Figure 11. Present-day temperature profile in the stagnant lid, in the north (black) and in the south (red), for models that show the best scores (i.e., that fit all our four constraints). The temperature profiles of the reference model (section 4.1, Figure 5) are shown in bold lines. The southern surface altitude ($r = R_p^S$) is illustrated by the horizontal black line and the base of the stagnant lid by the dashed lines. The shaded areas correspond to the range of temperature profile obtained in the simulations that have the best scores (between 2.5 and 2.91) for both the Uniform Crustal Model and Non-Uniform Crustal Model simulations.

of volatiles (Morschhauser et al., 2011). Our modeling does not provide a self-consistent way to investigate water depletion as it assumes that the bulk of the crust is formed at the beginning of our simulations. However, using a scenario of crustal formation by mantle partial melting, Morschhauser et al. (2011) found that a wet olivine rheology with a low reference viscosity is more compatible with the crustal formation history during the early stages of evolution, whereas the occurrence of present-day volcanism is better fitted with a mantle depleted in water due to crustal formation. Accounting for a more realistic crustal and volatile extraction process by mantle partial melting in our simulations might lead to lower elastic thicknesses during the Noachian period—still in agreement with our constraint–but would probably not significantly change our present-day values.

In our model, we consider diffusion creep deformation mechanisms in the mantle with an activation energy of 300 kJ/mol for a dry mantle (Karato & Wu, 1993). It is however not clear if dislocation creep rather than diffusion creep occurs in the Martian mantle. Simulations with a lower activation energy of 200 kJ/mol for dislocation creep and a dry olivine mantle rheology (see section 3.1) lead to thinner lithospheres. The constraint of present-day melting is thus more easily met, and models with even thinner crusts more enriched in radioelements are acceptable. Compared to results obtained with an activation energy of 300 kJ/mol, our best fits for both the UCM and NUCM simulations are obtained when considering thinner crusts by about 10 to 15 km that are less dense and more enriched in radioelements (see Figure 8 for detailed ranges of parameters).

5.4. Effect of the Initial Conditions

In our models the initial mantle temperature has an impact on the present-day elastic thickness in the case of a dry mantle rheology—that is, large viscosity—since the large enrichment of radiogenics in the crust and depletion in the mantle can lead to a less pronounced thermostat effect. In this case, the less vigorous convection in the strongly depleted mantle cannot entirely erase the difference in initial temperatures.

One-dimensional parameterized models of the coupled crustal and thermal evolution of Mars suggest that the initial mantle temperature would be about 1,700 K (Hauck & Phillips, 2002; Morschhauser et al., 2011), thus lower than that considered here (1,800 K). An initial temperature of 1,700 K leads to higher present-day T_e values by ~30 km on average and thicker stagnant lids in both hemispheres, hardly compatible with recent volcanism, especially for UCM simulations. Only a few NUCM parameter combinations considering a thick southern crust (~75–85 km), moderately enriched in radioelements (~7.8–9), fit our four constraints. Conversely, for a higher initial mantle temperature of 1,900 K, the four constraints are fitted with a similar mantle depletion as in the models presented in sections 5.1 and 5.2. For the NUCM simulations, using a temperature increase of 200 K rather than 100 K following the impact has the same effect as considering T_{m_0} = 1,900 K. The impact age—ranging from 4.5 to 4 Gyr—has only very little effect on our T_e evolution.

5.5. Predictions on Present-Day Thermal Structure

The results of our study suggest that the temperature profiles at the present day might be different in both hemispheres (Figure 11). For instance, our NUCM reference model (see section 4.1 for its crustal parameters, in bold on Figure 11) shows a temperature profile that might be higher by >300 K over more than 250 km depth in the southern hemisphere in comparison to the northern one. The surface temperature is considered the same in both hemispheres but the temperature gradient in the southern crust is much larger than in the north because of its larger thickness and radioelement content. The difference in temperature between the two hemispheres reaches its maximum at the depth of the southern crust-mantle transition and remains constant in the entire lithospheric mantle. These predictions on Mars's current thermal structure are quite stable among our best fit models (see Table 4 and shadowed areas on Figure 11 that represent the dispersion of their temperature profiles).

The future InSight NASA mission will land on Mars in the northern hemisphere, close to the dichotomy boundary in November 2018 and will place a seismometer (SEIS) and a heat flow probe (HP^3) on the planet's surface.

The north/south differences in thermal structure predicted by our models might thus leave a signature in the seismic signals recorded by the seismometer (Panning et al., 2014). Furthermore, both crustal models predict a similar surface heat flux at the InSight landing site in the north, with a range of 17.1 to 19.5 mW/m^2 for the best models. Heat flux are predicted to be significantly higher in the south with a range of 24.8–26.5 mW/m^2 (Table 4).

5.6. Model Limitations and Validation

Our model is limited because crustal properties are assumed to be homogeneous over an entire hemisphere, although spatial differences in thicknesses probably exist (Neumann et al., 2004). We also assume a well-mixed mantle, which does not account for upwellings and downwellings even though they induce spatial variability in lithosphere thickness. In fact, T_e estimates below the two polar caps might not be representative of the entire hemisphere as assumed here.

To validate our 1-D model, we compared our results with those obtained in 3-D convection simulations by Plesa et al. (2016) in a model setup accounting for a crustal model comparable to the UCM case presented here (case 25 of Plesa et al. (2016)). Strong mantle plumes cause lateral variations of 40 km for the present-day elastic thicknesses over a hemisphere, which is consistent with the assumptions we made for this study (see section 2 and Figure 2c). Furthermore, we found that there is a close agreement between our north/south temperature profiles and those of Plesa et al. (2016) averaged over each hemisphere. In particular, Plesa et al. (2016) also observe a similar north/south difference in temperature and retrieve present-day surface heat flux in good agreement with ours. Their total range of surface heat flux is larger (16.2–35.3 mW/m^2 and 19 mW/m^2 at the InSight landing site in their case 25, in comparison to a range of 17.1–26.5 mW/m^2 and 17.1 mW/m^2 at the InSight landing site for our model), but this is likely due to localized effects of the topography in the 3-D thermal simulations that cannot be resolved with our 1-D model.

6. Summary

The prominent north/south crustal dichotomy might extend at depth and induce distinct lithosphere thicknesses for the two hemispheres. We have therefore distinguished northern and southern T_e estimates and used three main constraints on T_e evolution: low values during the Noachian in the south and a potentially large north/south present-day difference below the two polar caps ($\geq$300 km in the north and $>$110 km in the south). As recent volcanic activity has been suggested for the large volcanic centers on Mars, suitable models must also allow for present-day melt formation in the highlands.

In our simulations, a dichotomy in crustal structure and composition was considered with two possible crustal models. The UCM case is characterized by a uniform crustal composition but the southern crust is thicker to compensate for the north/south difference in altitude. In the NUCM case, the southern crust can have distinct properties (conductivity, enrichment in radioelements, density and thickness) compared to the northern one.

Running Monte Carlo simulations with a parameterized thermal evolution model accounting for north/south differences in crustal properties, we find the range of crustal parameters that fit constraints on elastic lithosphere thickness and present-day volcanism. Interestingly, both the UCM and NUCM cases converge on similar ranges of values for the northern and southern crustal radioelement contents. In order to fit the large current northern T_e, we predict that 55–65% of the radioelements have to be concentrated in the crust, and more than 42% in the southern one, which implies a similar mantle depletion in water. In most suitable models, expected crustal thicknesses are higher than those usually assumed in the highlands, with northern and southern averages of 35 and 80 km, respectively, and a bulk average of 40–75 km, with a southern crust that is equally or slightly less dense than the northern one. Enrichment factors in radioelements are in the upper range of values or even slightly higher than in previous studies. However, simulations with two types of crust also show a high score for a southern crust much more enriched in radioelements than the north (by a factor of 2.2). These models are associated with a southern crust less dense than the northern one by as much as 480 kg/m^3 (in agreement with Pauer and Breuer (2008) and Baratoux et al. (2014)), which would suggest the presence of a buried felsic component in the south. Note that all of the results are given for a dry olivine mantle rheology. A present-day wet mantle rheology cannot satisfactorily fit the $\geq$300 km northern present-day elastic thickness constraint, which is coherent with the large mantle extraction of radioelements and volatiles predicted by our models. Conversely, both wet and dry diabase crustal rheologies are possible and converge to the same predictions regarding crustal properties.

The future InSight mission is expected to land close to the dichotomy boundary in the northern hemisphere. In our models north/south present-day thermal profiles are expected to differ by 170 to 304 K over more than 250–310 km depth, which might result in different travel times of seismic waves produced by events occurring in the two hemispheres and leave a signature in the geophysical signals recorded by the SEIS instrument. Surface heat flux should also be very different in between both hemispheres: we predict values as high as 24.8–26.5 mW/m^2 in the highlands and low heat flux in the range of 17.1–19.5 mW/m^2 in the north (that is, at the InSight landing site), close to those of Plesa et al. (2016) when considering similar crustal properties.

Appendix A: NUCM Simulations With a Variable Northern Enrichment Factor

In order to investigate the role of the Northern crustal parameters in more detail for the NUCM simulations, we also run Monte Carlo simulations where the northern crustal enrichment factor could vary between 5 and 15. We refer to these simulations as the Non-Uniform Crustal Model 2 (NUCM2). We found suitable parameter combinations, that fit the three T_e constraints and present-day melt formation, when considering northern crustal enrichment factor ranging from 5 to 13.5. However, in order to fit the large present-day elastic thickness in the north, the percentage of radioelements that could be concentrated in the northern crust remains very close to that retrieved by the UCM and NUCM cases (Figure 9b and Table 4). There is thus a trade-off between the enrichment factor and the thickness of the northern crust: the more enriched, the thinner the crust is. The ranges of enrichment factor retrieved for NUCM2 simulations correspond to surface concentrations of K and Th that are in agreement with GRS data.

Appendix B: Effect of a Wet or Dry Rheology for the Mantle and the Crust

Considering a dry mantle and dry crustal rheology also provides a good fit to the three T_e constraints. By using crustal models similar to our UCM case, Breuer et al. (2016) and Grott and Breuer (2008) found that a dry mantle and dry crustal rheology is not in agreement with the Noachian low T_e. Indeed, a dry crust is stronger and the thinner incompetent bottom crustal layer disappears earlier both in the north and in the south in Mars evolution. Nevertheless, they used crustal thicknesses of 30–60 km and an enrichment factor of 5–10, lower than the ranges considered here. In our simulations we find that models accounting for thicker crusts more enriched in radioelements could predict low elastic thicknesses during the Noachian period in agreement with our constraint, especially for the NUCM simulations as even more radioelements could be concentrated in the southern crust. The Noachian constraint remains however hard to fit for the UCM simulations where minimal values of 43 km are reached for the elastic thickness in the Noachian, that is, in the upper bound of Noachian estimates. Interestingly the range of suitable models for the southern Noachian constraint is similar to that fitting the present-day northern T_e. The present-day elastic thicknesses and their fit to the constraints remain similar to those for a wet crust and dry mantle. Our best fits for the dry mantle dry crustal rheology predict therefore similar parameters as those for the dry mantle and wet crustal one. For the UCM case, simulations with the best scores have crustal thicknesses of 31–39 km in the north, 89–101 km in the south, an enrichment factor of 7.9–9.1 and a crustal density of 3,138–3,182 kg/m^3 (Figure 10a). For the NUCM simulations, the northern crust is predicted to have a thickness of 30–45 km, for a radioelement enrichment of 10, and the southern one is 43–93 km thick with an enrichment factor of 8.4–21.7 and a density range of 2,620–3,100 kg.m^3 for its lower part (for 3,100 kg/m^3 in the north) (Figure 10b).

We also run Monte Carlo simulations with a wet mantle and a dry or wet crust. In this case, the mantle viscosity is lower and therefore energy transfer by convection is more efficient, resulting in thinner lithosphere thicknesses. In this context many models that were fitting constraints for a dry mantle, are now excluded because they predict crustal delamination due to high mantle temperatures during the early stages of evolution. We note that two parameters favor thin lithosphere thicknesses and delamination processes: a thick crust and/or a high crustal heat production. In UCM simulations, the southern crust is thick (at least 65 km) and therefore none of our simulations prevents crustal delamination. But for NUCM simulations, lower southern crustal thicknesses of 40–45 km in the south and ~30 km in the north can be found, which do not lead to delamination. These models have an enrichment factor of 6–8.6 in the lower south crust (for $\Lambda^N = 10$). In these simulations T_e are much thinner than for a dry mantle and there is therefore a good fit to the Noachian and the present-day southern constraints. Nevertheless, none of our simulations with a wet mantle rheology fit the high northern present-day T_e, and show maximum values of only 180 km.

Acknowledgments
We thank Alexandre Fournier, Cinzia Farnetani for helpful discussions as well as James Roberts, and an anonymous reviewer for their constructive comments.
The authors acknowledge the financial support of the UnivEarthS Labex program at Sorbonne Paris Cite (ANR-10-LABX-0023 and ANR-11-IDEX-0005-02) and of the German Academic Exchange Service (DAAD). All the numerical results shown in this work are available at https://figshare.com/projects/2017JE005431RR/29467. This is Insight Contribution Number 58.

References

Agee, C., Wilson, N., McCubbin, F., Ziegler, K., Polyak, V., Sharp, Z., et al. (2013). Unique meteorite from early Amazonian Mars: Water-rich basaltic breccia Northwest Africa 7034. *Science*, *339*, 780–785. https://doi.org/10.1126/science.1228858

Andrews-Hanna, J., Zuber, M., & Banerdt, W. (2008). The Borealis basin and the origin of the Martian crustal dichotomy. *Nature*, *453*, 1212–1215. https://doi.org/10.1038/nature07011

Aoudjehane, H., Avice, G., Barrat, J.-A., Boudouma, O., Chen, G., Duke, M., et al. (2012). Tissint Martian meteorite: A fresh look at the interior, surface, and atmosphere of Mars. *Science*, *338*, 785–788. https://doi.org/10.1126/science.1224514

Arkani-Hamed, J., & Olson, P. (2010). Giant impacts, core stratification, and failure of the Martian dynamo. *Journal of Geophysical Research*, *115*, E07012. https://doi.org/10.1029/2010JE003579

Bandfield, J., Edwards, C., Montgomery, D., & Brand, B. (2013). The dual nature of the Martian crust: Young lavas and old clastic materials. *Icarus*, *222*, 188–199. https://doi.org/10.1016/j.icarus.2012.10.023

Baratoux, D., Samuel, H., Michaut, C., Toplis, M., Monnereau, M., Wieczorek, M., et al. (2014). Petrological constraints on the density of the Martian crust. *Journal of Geophysical Research: Planets*, *119*, 1707–1727. https://doi.org/10.1002/2014JE004642

Baratoux, D., Toplis, M., Monnereau, M., & Gasnault, O. (2011). Thermal history of Mars inferred from orbital geochemistry of volcanic provinces. *Nature*, *472*, 338–341. https://doi.org/10.1038/nature09903

Barnett, D., & Nimmo, F. (2002). Strength of faults on Mars from MOLA topography. *Icarus*, *157*, 34–42. https://doi.org/10.1006/icar.2002.6817

Belleguic, V., Lognonné, P., & Wieczorek, M. (2005). Constraints on the Martian lithosphere from gravity and topography data. *Journal of Geophysical Research*, *110*, E11005. https://doi.org/10.1029/2005JE002437

Bottke, W., & Andrews-Hanna, J. (2017). A post-accretionary lull in large impacts on early Mars. *Nature Geoscience*, *10*, 344–348. https://doi.org/10.1038/ngeo2937

Brasser, R., & Mojzsis, S. (2017). A colossal impact enriched Mars' mantle with noble metals. *Geophysical Research Letters*, *44*, 5978–5985. https://doi.org/10.1002/2017GL074002

Breuer, D., & Spohn, T. (2006). Viscosity of the Martian mantle and its initial temperature: Constraints from crust formation history and the evolution of the magnetic field. *Planetary and Space Science*, *54*, 153–169. https://doi.org/10.1016/j.pss.2005.08.008

Breuer, D., Plesa, A.-C., Tosi, N., & Grott, M. (2016). Water in the Martian interior—The geodynamical perspective. *Meteoritics and Planetary Science*, *51*, 1959–1992. https://doi.org/10.1111/maps.12727

Burov, E., & Diament, M. (1995). The effective elastic thickness (t_e) of continental lithosphere: What does it really mean? *Journal of Geophysical Research*, *100*, 3905–3927. https://doi.org/10.1029/94JB02770

Byerlee, J. (1978). Friction of rocks. *Pure and Applied Geophysic*, *116*, 615–626. https://doi.org/10.1007/BF00876528

Caristan, Y. (1982). The transition from high temperature creep to fracture in Maryland diabase. *Journal of Geophysical Research*, *87*, 6781–6790. https://doi.org/10.1029/JB087iB08p06781

Carter, J., & Poulet, F. (2013). Ancient plutonic processes on Mars inferred from the detection of possible anorthositic terrains. *Nature Geoscience*, *6*, 1008–1012. https://doi.org/10.1038/NGEO1995

Christensen, P. (1983). Convection in a variable-viscosity fluid: Newtonian versus power-law rheology. *Earth and Planetary Science Letters*, *64*, 153–162. https://doi.org/10.1016/0012-821X(83)90060-2

Christensen, P., McSween, H., Bandfield, J. Jr., Ruff, S., Rogers, A., Hamilton, V., et al. (2005). Evidence for magmatic evolution and diversity on Mars from infrared observations. *Nature*, *436*, 504–509. https://doi.org/10.1038/nature03639

Clauser, C., & Huenges, E. (1995). Thermal conductivity of rocks and minerals. In T. J. Ahrens (Ed.), *Rock physics and phase relations: A handbook of physical constants* (pp. 105–126). Washington, DC: American Geophysical Union. https://doi.org/10.1029/RF003p0105

Davaille, A., & Jaupart, C. (1993). Transient high-Rayleigh-number thermal convection with large viscosity variations. *Journal of Fluid Mechanics*, *253*, 141–166.

Deschamps, F., & Sotin, C. (2000). Inversion of two-dimensional numerical convection experiments for a fluid with a strongly temperature-dependent viscosity. *Geophysical Journal International*, *143*, 204–218. https://doi.org/10.1046/j.1365-246x.2000.00228.x

Durham, W., & Goetze, C. (1977a). Plastic flow of oriented single crystals of olivine: 1. Mechanical data. *Journal of Geophysical Research*, *82*, 5737–5753. https://doi.org/10.1029/JB082i036p05737

Durham, W., & Goetze, C. (1977b). A comparison of the creep properties of pure forsterite and iron-bearing olivine. *Tectonophysics*, *40*, 15–18. https://doi.org/10.1016/0040-1951(77)90063-4

Elkins-Tanton, L., Hess, P., & Parmentier, E. (2005). Possible formation of ancient crust on Mars through magma ocean processes. *Journal of Geophysical Research*, *110*, E12S01. https://doi.org/10.1029/2005JE002480

Elkins-Tanton, L., Parmentier, E., & Hess, P. (2003). Magma ocean fractional crystallization and cumulate overturn in terrestrial planets: Implications for Mars. *Meteoritics and Planetary Science*, *38*, 1753–1771. https://doi.org/10.1111/j.1945-5100.2003.tb00013.x

Frey, H. (2008). Ages of very large impact basins on Mars: Implications for the late heavy bombardment in the inner solar system. *Geophysical Research Letters*, *35*, L13203. https://doi.org/10.1029/2008GL033515

Gagnepain-Beyneix, J., Lognonné, P., Chenet, H., Lombardi, D., & Spohn, T. (2006). A seismic model of the lunar mantle and constraints on temperature and mineralogy. *Physics of the Earth and Planetary Interiors*, *159*, 140–166. https://doi.org/10.1016/j.pepi.2006.05.009

Golabek, G., Keller, T., Gerya, T., Zhu, G., Tackley, P., & Connolly, J. (2011). Origin of the Martian dichotomy and Tharsis from a giant impact causing massive magmatism. *Icarus*, *215*, 346–357. https://doi.org/10.1016/j.icarus.2011.06.012

Goossens, S., Sabaka, T., Genova, A., Mazarico, E., Nicholas, J., & Neumann, G. (2017). Evidence for a low bulk crustal density for Mars from gravity and topography. *Geophysical Research Letters*, *44*, 7686–7694. https://doi.org/10.1002/2017GL074172

Grasset, O., & Parmentier, E. (1998). Thermal convection in a volumetrically heated, infinite Prandtl number fluid with strongly temperature-dependent viscosity: Implications for planetary thermal evolution. *Journal of Geophysical Research*, *103*, 18,171–18,181. https://doi.org/10.1029/98JB01492

Grott, M. (2005). Late crustal growth on Mars: Evidence from lithospheric extension. *Geophysical Research Letters*, *32*, L23201. https://doi.org/10.1029/2005GL024492

Grott, M., & Breuer, D. (2008). The evolution of the Martian elastic lithosphere and implications for crustal and mantle rheology. *Icarus*, *193*, 503–515. https://doi.org/10.1016/j.icarus.2007.08.015

Grott, M., & Breuer, D. (2009). Implications of large elastic thicknesses for the composition and current thermal state of Mars. *Icarus*, *201*, 540–548. https://doi.org/10.1016/j.icarus.2009.01.020

Grott, M., & Breuer, D. (2010). On the spatial variability of the Martian elastic lithosphere thickness: Evidence for mantle plumes? *Journal of Geophysical Research*, *115*, E03005. https://doi.org/10.1029/2009JE003456

Grott, M., Baratoux, D., Hauber, E., Sautter, V., Mustard, J., Gasnault, O., et al. (2013). Long-term evolution of the Martian crust-mantle system. *Space Science Reviews*, *174*, 49–111. https://doi.org/10.1007/s11214-012-9948-3

Grott, M., Hauber, E., Werner, S., Kronberg, P., & Neukum, G. (2005). High heat flux on ancient Mars: Evidence from rift flank uplift at Coracis Fossae. *Geophysical Research Letters*, *32*, L21201. https://doi.org/10.1029/2005GL023894

Grott, M., Hauber, E., Werner, S., Kronberg, P., & Neukum, G. (2007). Mechanical modeling of thrust faults in the Thaumasia region, Mars, and implications for the Noachian heat flux. *Icarus*, *186*, 517–526. https://doi.org/10.1016/j.icarus.2006.10.001

Grott, M., Morschhauser, A., breuer, D., & Hauber, E. (2011). Volcanic outgassing of CO_2 and H_2O on Mars. *Earth and Planetary Science Letters*, *308*, 391–400. https://doi.org/10.1016/j.epsl.2011.06.014

Hartmann, W., & Malin, D. (2000). Elysium Planitia lava flows: Crater count chronology and geological implications. *Journal of Geophysical Research*, *105*, 15,011–15,025. https://doi.org/10.1029/1999JE001189

Hartmann, W., Malin, M., McEwen, A., Carr, M., Soderblom, L., Thomas, P., et al. (1999). Evidence for recent volcanism on Mars from crater counts. *Nature*, *397*, 586–589. https://doi.org/10.1038/17545

Hauber, E., Bleacher, J., Gwinner, K., Williams, D., & Greeley, R. (2009). The topography and morphology of low shields and associated landforms of plains volcanism in the Tharsis region of Mars. *Journal of Volcanology and Geothermal Research*, *185*, 69–95. https://doi.org/10.1016/j.jvolgeores.2009.04.015

Hauber, E., Brož, P., Jabert, F., Jodlowski, P., & Platz, T. (2011). Very recent and wide-spread basaltic volcanism on Mars. *Geophysical Research Letters*, *38*, L10201. https://doi.org/10.1029/2011GL047310

Hauck, S., & Phillips, R. (2002). Thermal and crustal evolution of Mars. *Journal of Geophysical Research*, *107*, E75052. https://doi.org/10.1029/2001JE001801

Hoogenboom, T., & Smrekar, S. (2006). Elastic thickness estimates for the northern lowlands of Mars. *Earth and Planetary Science Letters*, *248*, 830–839. https://doi.org/10.1002/2014GL061779

Huang, J., & Xiao, L. (2014). Knobby terrain on ancient volcanoes as an indication of dominant early explosive volcanism on Mars. *Geophysical Research Letters*, *41*, 7019–7024. https://doi.org/10.1002/2014GL061779

Humayun, M., Nemchin, A., Zanda, B., Hewins, R. H., Grange, M., Kennedy, A., et al. (2013). Origin and age of the earliest Martian crust from meteorite NWA 7533. *Nature*, *503*, 513–517. https://doi.org/10.1038/nature12764

Jagoutz, E. (1991). Chronology of SNC meteorites. *Space Science Reviews*, *56*, 13–22. https://doi.org/10.1007/BF00178386

Karato, S.-I., & Wu, P. (1993). Rheology of the upper mantle: A synthesis. *Science*, *260*, 771–778. https://doi.org/10.1126/science.260.5109.771

Ke, Y., & Solomatov, V. (2009). Coupled core-mantle thermal evolution of early Mars. *Journal of Geophysical Research*, *114*, E07004. https://doi.org/10.1029/2008JE003291

Kiefer, W. (2004). Gravity evidence for an extinct magma chamber beneath Syrtis Major, Mars: A look at the magmatic plumbing system. *Earth and Planetary Science Letters*, *222*, 349–361. https://doi.org/10.1016/j.epsl.2006.06.035

Kiefer, W., & Li, Q. (2009). Mantle convection controls the observed lateral variations in lithospheric thickness on present-day Mars. *Geophysical Research Letters*, *36*, L18203. https://doi.org/10.1029/2009GL039827

Kiefer, W., Filiberto, J., Sandu, C., & Li, Q. (2015). The effects of mantle composition on the peridotite solidus: Implications for the magmatic history of Mars. *Geochimica et Cosmochimica Acta*, *162*, 247–258. https://doi.org/10.1016/j.gca.2015.02.010

Konopliv, A., Yoder, C., Standish, E., Yuan, D.-N., & Sjogren, W. (2006). A global solution for the Mars static and seasonal gravity, Mars orientation, Phobos and Deimos masses, and Mars ephemeris. *Icarus*, *182*, 23–50. https://doi.org/10.1016/j.icarus.2005.12.025

Kronberg, P., Hauber, E., Grott, M., Werner, S., Schäfer, T., Gwinner, K., et al. (2007). Acheron Fossae, Mars: Tectonic rifting, volcanism, and implications for lithospheric thickness. *Journal of Geophysical Research*, *112*, E04005. https://doi.org/10.1029/2006JE002780

Laskar, J., Robutel, P., Joutel, F., Gastineau, M., Correia, A., & Levrard, B. (2004). A long-term numerical solution for the insolation quantities of the Earth. *Astronomy and Astrophysics*, *428*, 261–285. https://doi.org/10.1051/0004-6361:20041335

Leone, G., Tackley, P., Gerya, T., May, D., & Zhu, G. (2014). Three-dimensional simulations of the southern polar giant impact hypothesis for the origin of the Martian dichotomy. *Geophysical Research Letters*, *41*, 8736–8743. https://doi.org/10.1002/2014GL062261

Li, Q., & Kiefer, W. (2007). Mantle convection and magma production on present-day Mars: Effects of temperature-dependent rheology. *Geophysical Research Letters*, *34*, L16203. https://doi.org/10.1029/2007GL030544

Mackwell, S., Zimmerman, M., & Kohlstedt, D. (1998). High-temperature deformation of dry diabase with application to tectonics on Venus. *Journal of Geophysical Research*, *103*, 975–984. https://doi.org/10.1029/97JB02671

Marinova, M., Aharonson, O., & Asphaug, E. (2008). Mega-impact formation of the Mars hemispheric dichotomy. *nature*, *453*, 1216–1219. https://doi.org/10.1038/nature07070

McGovern, P., Solomon, S., Smith, D., Zuber, M., Simons, M., Wieczorek, M., et al. (2004). Correction to 'localized gravity/topography admittance and correlation spectra on Mars: Implications for regional and global evolution'. *Journal of Geophysical Research*, *109*, E07007. https://doi.org/10.1029/2004JE002286

McNutt, M., Diament, M., & Kogan, M. (1988). Variations of elastic plate thickness at continental thrust belts. *Journal of Geophysical Research*, *93*, 8825–8838. https://doi.org/10.1029/JB093iB08p08825

McSween, H., Wyatt, M., Gellert, R., Bell III, J., Morris, R., Herkenhoff, K., et al. (2006). Characterization and petrologic interpretation of olivine-rich basalts at Gusev Crater, Mars. *Journal of Geophysical Research*, *111*, E02S10. https://doi.org/10.1029/2005JE002477

McSween, H. Jr., Grove, T., Lentz, R., Dann, J., Holzheid, A., Riciputi, L., et al. (2001). Geochemical evidence for magmatic water within Mars from pyroxenes in the Shergotty meteorite. *Nature*, *409*, 487–490. https://doi.org/10.1038/35054011

Médard, E., & Grove, T. (2006). Early hydrous melting and degassing of the Martian interior. *Journal of Geophysical Research*, *111*, E11003. https://doi.org/10.1029/2006JE002742

Mei, S., & Kohlstedt, D. (2000a). Influence of water on plastic deformation of olivine aggregates: 1. Diffusion creep regime. *Journal of Geophysical Research*, *105*, 21,457–21,469. https://doi.org/10.1029/2000JB900179

Mei, S., & Kohlstedt, D. (2000b). Influence of water on plastic deformation of olivine aggregates: 2. Dislocation creep regime. *Journal of Geophysical Research*, *105*, 21,471–21,481. https://doi.org/10.1029/2000JB900180

Mellon, M., Feldman, W., & Prettyman, T. (2004). The presence and stability of ground ice in the southern hemisphere of Mars. *Icarus*, *169*(2), 324–340. https://doi.org/10.1016/j.icarus.2003.10.022

Michaut, C., & Jaupart, C. (2004). Nonequilibrium temperatures and cooling rates in thick continental lithosphere. *Geophysical Research Letters*, *31*, L24602. https://doi.org/10.1029/2004GL021092

Morschhauser, A., Grott, M., & Breuer, D. (2011). Crustal recycling, mantle dehydration, and the thermal evolution of Mars. *Icarus*, *212*, 541–558. https://doi.org/10.1016/j.icarus.2010.12.028

Mueller, S., & Phillips, R. (1995). On the reliability of lithospheric constraints derived from models of outer-rise flexure. *Journal of Geophysical Research*, *123*, 887–902. https://doi.org/10.1111/j.1365-246x.1995.tb06896.x

Mustard, J., Poulet, F., Gendrin, A., Bibring, J.-P., Langevin, Y., Gondet, B., et al. (2005). Olivine and pyroxene diversity in the crust of Mars. *Science*, *307*, 1594–1597. https://doi.org/10.1126/science.1109098

Neukum, G., Jaumann, R., Hoffmann, H., Hauber, E., Head, J., Basilevsky, A., et al. (2004). Recent and episodic volcanic and glacial activity on Mars revealed by the High Resolution Stereo Camera. *Nature*, *432*, 971–979. https://doi.org/10.1038/nature03231

Neumann, G., Zuber, M., Wieczorek, M., McGovern, P., Lemoine, F., & Smith, D. (2004). Crustal structure of Mars from gravity and topography. *Journal of Geophysical Research*, *109*, E08002. https://doi.org/10.1029/2004JE002262

Nimmo, F., & Stevenson, D. (2001). Estimates of Martian crustal thickness from viscous relaxation of topography. *Journal of Geophysical Research*, *106*, 5085–5098. https://doi.org/10.1029/2000JE001331

Nimmo, F., & Tanaka, K. (2005). Early crustal evolution of Mars. *Annual Reviews Earth and Planetary Sciences*, *33*, 133–161. https://doi.org/10.1146/annurev.earth.33.092203.122637

Nyquist, L., Bogart, D., Shih, C.-Y., Greshake, A., Stöffler, D., & Eugster, O. (2001). Ages and geologic histories of Martian meteorites. *Space Science Reviews*, *96*, 105–164. https://doi.org/10.1023/A:1011993105172

O'Neill, C., Lenardic, A., Jellinek, A. M., & Kiefer, W. S. (2007). Melt propagation and volcanism in mantle convection simulations, with applications for Martian volcanic and atmospheric evolution. *Journal of Geophysical Research*, *112*, E07003. https://doi.org/10.1029/2006JE002799

Panning, M., Beucler, E., Drilleau, M., Mocquet, A., Lognonné, P., & Banerdt, W. (2014). Verifying single-station seismic approaches using Earth-based data: Preparation for data return from the InSight mission to Mars. *Icarus*, *248*, 230–242. https://doi.org/10.1016/j.icarus.2014.10.035

Papike, J., Karner, J., Shearer, C., & Burger, P. (2009). Silicate mineralogy of Martian meteorites. *Geochimica et Cosmochimica Acta*, *73*, 7443–7485. https://doi.org/10.1016/j.gca.2009.09.008

Parmentier, E., & Zuber, M. (2007). Early evolution of Mars with mantle compositional stratification or hydrothermal crustal cooling. *Journal of Geophysical Research*, *112*, E02007. https://doi.org/10.1029/2005JE002626

Pauer, M., & Breuer, D. (2008). Constraints on the maximum crustal density from gravity topography modeling: Applications to the southern highlands of Mars. *Earth and Planetary Science Letters*, *276*, 253–261.

Phillips, R., Zuber, M., Smrekar, S., Mellon, M., Head, J., Tanaka, K., et al. (2008). Mars north polar deposits: Stratigraphy, age, and geodynamical response. *Science*, *320*, 1182–1185. https://doi.org/10.1126/science.1157546

Piqueux, S., & Christensen, P. (2009a). A model of thermal conductivity for planetary soils: 1. Theory for unconsolidated soils. *Journal of Geophysical Research*, *114*, E09005. https://doi.org/10.1029/2008JE003308

Piqueux, S., & Christensen, P. (2009b). A model of thermal conductivity for planetary soils: 2. Theory for cemented soils. *Journal of Geophysical Research*, *114*, E09006. https://doi.org/10.1029/2008JE003309

Plesa, A.-C., Grott, M., Tosi, N., Breuer, D., Spohn, T., & Wieczorek, M. (2016). How large are present-day heat flux variations across the surface of Mars?*Geophysical Research Planets*, *121*, 2386–2403. https://doi.org/10.1002/2016JE005126

Reese, C., Orth, C., & Solomatov, V. (2010). Impact origin for the Martian crustal dichotomy: Half emptied or half filled? *Journal of Geophysical Research*, *115*, E05004. https://doi.org/10.1029/2009JE003506

Richter, F. (1978). Mantle convection models. *Annual Review of Earth and Planetary Sciences*, *6*, 9–19. https://doi.org/10.1146/annurev.ea.06.050178.000301

Ritzer, J., & Hauck, S. (2009). Lithospheric structure and tectonics at Isidis Planitia, Mars. *Icarus*, *201*, 528–539. https://doi.org/10.1016/j.icarus.2009.01.025

Roberts, J., & Arkani-Hamed, J. (2014). Impact heating and coupled core cooling and mantle dynamics on Mars. *Journal of Geophysical Research: Planets*, *119*, 729–744. https://doi.org/10.1002/2013JE004603

Roberts, J., & Zhong, S. (2006). Degree-1 convection in the Martian mantle and the origin of the hemispheric dichotomy. *Journal of Geophysical Research*, *111*, E06013. https://doi.org/10.1029/2005JE002668

Ruiz, J., Fernández, C., Gomez-Ortiz, D., Dohm, J., López, V., & Tejero, R. (2008). Ancient heat flow, crustal thickness, and lithospheric mantle rheology in the Amenthes region, Mars. *Earth and Planetary Science Letters*, *270*, 1–12. https://doi.org/10.1016/j.epsl.2008.02.015

Sautter, V., Toplis, M., Wiens, R., Cousin, A., Fabre, C., Gasnault, O., et al. (2015). In situ evidence for continental crust on early Mars. *Nature Geoscience*, *8*, 605–611. https://doi.org/10.1038/NGEO2474

Schubert, G., & Spohn, T. (1990). Thermal history of Mars and the sulfur content of its core. *Journal of Geophysical Research*, *95*, 14,095–14,104. https://doi.org/10.1029/JB095iB09p14095

Schultz, R., & Watters, T. (2001). Forward mechanical modeling of the Amenthes Rupes thrust fault on Mars. *Geophysical Research Letters*, *28*, 4659–4662. https://doi.org/10.1029/2001GL013468

Schumacher, S., & Breuer, D. (2006). Influence of a variable thermal conductivity on the thermochemical evolution of Mars. *Journal of Geophysical Research*, *111*, E02006. https://doi.org/10.1029/2005JE002429

Seipold, U. (1998). Temperature dependence of thermal transport properties of crystalline rocks a general law. *Tectonophysics*, *291*, 161–171. https://doi.org/10.1016/S0040-1951(98)00037-7

Sekhar, P., & King, S. (2014). 3D spherical models of Martian mantle convection constrained by melting history. *Earth and Planetary Science Letters*, *388*, 27–37. https://doi.org/10.1016/j.epsl.2013.11.047

Solomon, S., Aharonson, O., Aurnou, J., Banerdt, W., Carr, M., Dombard, A., et al. (2005). New perspectives on ancient Mars. *Science*, *307*, 1214–1220. https://doi.org/10.1126/science.1101812

Stevenson, D., Spohn, T., & Schubert, G. (1983). Magnetism and thermal evolution of the terrestrial planets. *Icarus*, *54*, 466–489. https://doi.org/10.1016/0019-1035(83)90241-5

Susko, D., Karunatillake, S., Kodikara, G., Skok, J., Wray, J., Heldmann, J., et al. (2017). A record of igneous evolution in Elysium, a major Martian volcanic province. *Scientific Reports*, *7*, 43177. https://doi.org/10.1038/srep43177

Takahashi, E. (1990). Speculations on the Archean Mantle: Missing link between komatiite and depleted garnet peridotite. *Journal of Geophysical Research*, *95*, 15,941–15,954. https://doi.org/10.1029/JB095iB10p15941

Tanaka, K., Robbins, S., Fortezzo, C., Skinner, J. Jr., & Hare, T. (2014). The digital global geologic map of Mars: Chronostratigraphic ages, topographic and crater morphologic characteristics, and updated resurfacing history. *Planetary and Space Science*, *95*, 11–24. https://doi.org/10.1016/j.pss.2013.03.006

Taylor, G., Boynton, W., Brückner, J., Wänke, H., Dreibus, G., Kerry, K., et al. (2006). Bulk composition and early differentiation of Mars. *Journal of Geophysical Research*, *111*, E03S10. https://doi.org/10.1029/2005JE002645

Turcotte, D., & Schubert, G. (2002). *Geodynamics* (2nd ed., 456 pp.). New York: Cambridge University Press.

Vaucher, J., Baratoux, D., Mangold, N., Pinet, P., Kurita, K., & Gregoire, M. (2009). The volcanic history of central Elysium Planitia: Implications for Martian magmatism. *Icarus*, *204*, 418–442. https://doi.org/10.1016/j.icarus.2009.06.032

Wänke, H., & Dreibus, G. (1994). Chemistry and accretion history of Mars. *Philosophical Transactions: Physical Sciences and Engineering*, *349*, 285–293. https://doi.org/10.1098/rsta.1994.0132

Warner, N., Golombek, M. P., Sweeney, J., Fergason, R., Kirk, R., & Schwartz, C. (2017). Near surface stratigraphy and regolith production in southwestern Elysium Planitia, Mars: Implications for Hesperian-Amazonian terrains and the InSight Lander Mission. *Space Science Reviews*, *211*, 1–44. https://doi.org/10.1007/s11214-017-0352-x

Werner, S. (2009). The global Martian volcanic evolutionary history. *Icarus*, *201*, 44–68. https://doi.org/10.1016/j.icarus.2008.12.019

Wieczorek, M. (2008). Constraints on the composition of the Martian south polar cap from gravity and topography. *Icarus*, *196*, 506–517. https://doi.org/10.1016/j.icarus.2007.10.026

Wieczorek, M., & Zuber, M. (2004). Thickness of the Martian crust: Improved constraints from geoid-to-topography ratios. *Journal of Geophysical Research*, *109*, E01009. https://doi.org/10.1029/2003JE002153

Wray, J., Hansen, S., Dufek, J., Swayze, G., Murchie, S., Seelos, F., et al. (2013). Prolonged magmatic activity on Mars inferred from the detection of felsic rocks. *Nature Geoscience*, *6*, 1013–1017. https://doi.org/10.1038/NGEO1994

Xiao, L., Huang, J., Christensen, P., Greeley, R., Williams, D., Zhao, J., & He, Q. (2012). Ancient volcanism and its implication for thermal evolution of Mars. *Earth and Planetary Science Letters*, *323-324*, 9–18. https://doi.org/10.1016/j.epsl.2012.01.027

Yoshida, M., & Kageyama, A. (2006). Low-degree mantle convection with strongly temperature- and depth-dependent viscosity in a three-dimensional spherical shell. *Journal of Geophysical Research*, *111*, B03412. https://doi.org/10.1029/2005JB003905

Zuber, M., Solomon, S., Phillips, R., Smith, D., Tyler, G., Aharonson, O., et al. (2000). Internal structure and early thermal evolution of Mars from Mars Global Surveyor topography and gravity. *Science*, *287*, 1788–1793. https://doi.org/10.1126/science.287.5459.1788